

DNA 4424T

AD A 053463

MULTIPLE PHASE-SCREEN PROPAGATION ANALYSIS FOR DEFENSE SATELLITE COMMUNICATIONS SYSTEM

D.L. Knepp

Mission Research Corporation
735 State Street
Santa Barbara, California 93101

September 1977

Topical Report for Period November 1975—September 1977

CONTRACT No. DNA 001-76-C-0135

APPROVED FOR PUBLIC RELEASE;
DISTRIBUTION UNLIMITED.

AD NO. _____
DDC FILE COPY

THIS WORK SPONSORED BY THE DEFENSE NUCLEAR AGENCY
UNDER RDT&E RMSS CODE B323076464 S99QAXHB05405 H2590D.

Prepared for
Director
DEFENSE NUCLEAR AGENCY
Washington, D. C. 20305

DDC
RECEIVED
MAY 9 1978
B

(18) DNA, SBIE

(19) 4424T, AD E300 190

UNCLASSIFIED

SECURITY CLASSIFICATION OF THIS PAGE (When Data Entered)

REPORT DOCUMENTATION PAGE		READ INSTRUCTIONS BEFORE COMPLETING FORM
1. REPORT NUMBER DNA 4424T✓	2. GOVT ACCESSION NO.	3. RECIPIENT'S CATALOG NUMBER
4. TITLE (and Subtitle) MULTIPLE PHASE-SCREEN PROPAGATION ANALYSIS FOR DEFENSE SATELLITE COMMUNICATIONS SYSTEM.		5. TYPE OF REPORT & PERIOD COVERED Topical Report. Nov 75-Sep 77.
7. AUTHOR(s) D. L. Knepp		6. PERFORMING ORG. REPORT NUMBER MRC-R-332
9. PERFORMING ORGANIZATION NAME AND ADDRESS Mission Research Corporation 735 State Street Santa Barbara, California 93101		8. CONTRACT OR GRANT NUMBER(s) DNA 001-76-C-0135
11. CONTROLLING OFFICE NAME AND ADDRESS Director Defense Nuclear Agency Washington, D.C. 20305		10. PROGRAM ELEMENT, PROJECT, TASK AREA & WORK UNIT NUMBERS NWED Subtask S99QAXHB054-05
14. MONITORING AGENCY NAME & ADDRESS (if different from Controlling Office)		12. REPORT DATE Sep 77
		13. NUMBER OF PAGES 88
		15. SECURITY CLASS (of this report) UNCLASSIFIED
		15a. DECLASSIFICATION/DOWNGRADING SCHEDULE
16. DISTRIBUTION STATEMENT (of this Report) Approved for public release; distribution unlimited.		
17. DISTRIBUTION STATEMENT (of the abstract entered in Block 20, if different from Report)		
18. SUPPLEMENTARY NOTES This work sponsored by the Defense Nuclear Agency under RDT&E RMSS Code B323076464 S99QAXHB05405 H2590D.		
19. KEY WORDS (continue on reverse side if necessary and identify by block number) Scintillation Satellite Communication Propagation in Striated Media Defense Satellite Communications System		
20. ABSTRACT (continue on reverse side if necessary and identify by block number) This report presents and analyzes simulated results for electric field propa- gation through a thick, extended region of high-altitude striations of electron density. The simulated results correspond to the problem of communication from a JSCS satellite to a ground station at a frequency of 7.5 GHz. Statistical results are presented for S_4 scintillation index and intensity correlation length for a power-law and an exponential phase-screen PSD for values of phase standard deviation σ ranging from 1 to 100 radians and phase correlation length ρ ranging from 1 to 10 km.		

DD FORM 1473

1 JAN 73 EDITION OF 1 NOV 65 IS OBSOLETE

UNCLASSIFIED

SECURITY CLASSIFICATION OF THIS PAGE (When Data Entered)

406 548

Lee

UNCLASSIFIED

SECURITY CLASSIFICATION OF THIS PAGE(When Data Entered)

20. Abstract (Continued)

Examples of specific realizations of the electric field amplitude and phase at the receiver are also shown. These realizations of signal structure are being used in simulations of DSCS receiver operation, reported elsewhere.

ACCESSION for	
NTIS	White Section <input checked="" type="checkbox"/>
DDC	Buff Section <input type="checkbox"/>
UNANNOUNCED	<input type="checkbox"/>
JUSTIFICATION _____	
BY _____	
DISTRIBUTION/AVAILABILITY CODES	
Dist.	Avail. 1/ or SPECIAL
A	

UNCLASSIFIED

SECURITY CLASSIFICATION OF THIS PAGE(When Data Entered)

CONTENTS

<u>SECTION</u>		<u>PAGE</u>
	LIST OF FIGURES	2
1.0	INTRODUCTION	5
2.0	DIFFRACTION BY A GAUSSIAN LENS	10
	2.1 Gaussian Lens - Code Calculation	10
	2.2 Gaussian Lens - Analytic Results	11
3.0	DIFFRACTION BY A RANDOM THIN PHASE-SCREEN	15
4.0	DSCS SIMULATION RESULTS	21
	4.1 Simulation Results - 1 kilometer Correlation Length	26
	4.2 Simulation Results - 3 kilometer Correlation Length	35
	4.3 Simulation Results - 10 kilometer Correlation Length	43
5.0	CONCLUSIONS	51
	BIBLIOGRAPHY	52
APPENDIX A	MULTIPLE PHASE-SCREEN CODE	53
	A.1 Scalar Wave Equation Solution	53
	A.2 Generation of the Random Phase Screen	57
APPENDIX B	RELATIONSHIP BETWEEN PHASE AND ELECTRON NUMBER DENSITY	63
	B.1 Phase Screen PSD Related to Electron Density PSD	63
	B.2 One, Two and Three Dimensional Power Spectra	65
	B.3 Two Dimensional K^{-2} in-situ N_e Spectrum	68
	B.4 Two-dimensional Exponential in-situ N_e Spectrum	69
APPENDIX C	PHASE-SCREEN REALIZATIONS	71

FIGURES

<u>FIGURE</u>		<u>PAGE</u>
1	Geometry of DSCS simulation.	7
2(a)	Diffraction pattern of a Gaussian lens.	12
2(b)	Diffraction pattern of a Gaussian lens.	13
3	Comparison of intended phase-screen power spectral density with that generated by the simulation.	16
4	Intensity PSD as a function of distance from a thin Gaussian phase-screen.	18
5	S_4 scintillation index for Gaussian spectrum.	19
6	S_4 scintillation index vs σ_ϕ as a function of phase-screen PSD and correlation length.	24
7	Signal intensity correlation distance versus σ_ϕ as a function of phase-screen PSD and correlation length.	25
8	Comparison of simulation generated phase-screen PSD's for correlation length $\ell_c = 1$ km.	27
9	Realizations of signal intensity for power-law PSD with $\ell_c = 1$ km.	28
10	Realizations of signal intensity for exponential PSD with $\ell_c = 1$ km.	29
11	Realizations of signal phase for power-law PSD with $\ell_c = 1$ km.	30
12	Realizations of signal phase for exponential PSD with $\ell_c = 1$ km.	31
13	Intensity PSD for power-law phase-screen PSD with $\ell_c = 1$ km.	32
14	Intensity PSD for exponential phase-screen PSD with $\ell_c = 1$ km.	33
15	Comparison of simulation generated phase-screen PSD's for correlation length $\ell_c = 3$ km.	36

Figures (continued)

<u>FIGURE</u>		<u>PAGE</u>
16	Realizations of signal intensity for power-law PSD with $\ell_c = 3$ km.	37
17	Realizations of signal intensity for exponential PSD with $\ell_c = 3$ km.	38
18	Realizations of signal phase for power-law PSD with $\ell_c = 3$ km.	39
19	Realizations of signal phase for exponential PSD with $\ell_c = 3$ km.	40
20	Intensity PSD for power-law phase-screen PSD with $\ell_c = 3$ km.	41
21	Intensity PSD for exponential phase-screen PSD with $\ell_c = 3$ km.	42
22	Comparison of simulation generated phase-screen PSD's for correlation length $\ell_c = 10$ km.	44
23	Realizations of signal intensity for power-law PSD with $\ell_c = 10$ km.	45
24	Realizations of signal intensity for exponential PSD with $\ell_c = 10$ km.	46
25	Realizations of signal phase for power-law PSD with $\ell_c = 10$ km.	47
26	Realizations of signal phase for exponential PSD with $\ell_c = 10$ km.	48
27	Intensity PSD for power-law phase-screen PSD with $\ell_c = 10$ km.	49
28	Intensity PSD for exponential phase-screen PSD with $\ell_c = 10$ km.	50
C-1(a)	Realizations of phase-screens with exponential PSD.	73
C-1(b)	Realizations of phase-screens with exponential PSD.	74
C-1(c)	Realizations of phase-screens with exponential PSD.	75
C-1(d)	Realizations of phase-screens with exponential PSD.	76

Figures (continued)

<u>FIGURE</u>		<u>PAGE</u>
C-2(a)	Realizations of intensity at each observation screen location.	77
C-2(b)	Realizations of intensity at each observation screen location.	78
C-2(c)	Realizations of intensity at each observation screen location.	79
C-2(d)	Realizations of intensity at each observation screen location.	80
C-3	Analytic diffraction pattern of a Gaussian lens as a function of distance Z from the lens.	81

SECTION 1

1.0 INTRODUCTION

The problem of communication from a satellite to a ground station in the presence of large, spatially extended regions of high-altitude nuclear burst produced striations of electron density can be modeled as the problem of propagation through a thick medium composed of random index-of-refraction fluctuations. Since no general analytical solution is available for this problem it must be handled numerically. In this report, a multiple phase-screen propagation simulation is developed as a method to propagate electromagnetic waves through statistically chosen realizations of the random medium.

In general, the electron density striations are represented by a number of phase screens which are chosen to possess the same statistical description as the original striations. A plane wave is then propagated from one phase screen to the next until a solution for the electric field in the receiver plane is obtained. To obtain the statistics of the received field, the problem is solved a number of times with different realizations of the phase screens (all with the same statistics) and the results are averaged.

The possibility of generating and retaining the realizations of the received electric field is an advantage of this type of simulation solution particularly when the results are to be used in conjunction with a receiver simulation of the ground station electronics. For all the work reported here several realizations of the received field were retained and are available for future analysis.

This report considers the effect of nuclear burst produced striation structure on propagation of 7.5 GHz (wavelength = 0.04 m) communication signals from a satellite to a ground station. The two different geometries relevant to the Defense Satellite Communications System (DSCS) considered are shown in Figure 1 (a) for the case of striations ranging in altitude from 300 km (F region altitude) to 15000 km and case (b) for striations ranging from 6000 km to 15000 km altitude. In both cases the striations are assumed to be elongated in the direction perpendicular to the page so that there is no variation in the y-direction. All results are given in terms of the one dimensional phase-screen power spectral density or autocorrelation function. The relationship of these quantities to the electron density power spectral density is given in Appendix B. The choice of phase-screen power spectral density is arbitrary but for this work results were obtained for two spectra:

$$\phi_{\phi}^{(1)}(K) = \frac{\sigma_{\phi}^2 L_0}{2} \frac{1}{(1+K^2 L_0^2)^{3/2}} \quad (1-1)$$

$$\phi_{\phi}^{(2)}(K) = \sigma_{\phi}^2 \frac{L_0}{2} e^{-|K|L_0} \quad (1-2)$$

As shown in Appendix B $\phi_{\phi}^{(1)}$ corresponds to a K^{-2} power law spectral density for one-dimensional electron density fluctuations (thought to be representative of the ambient ionosphere) and $\phi_{\phi}^{(2)}$ corresponds to a one-dimensional exponential (or Chesnut) power spectral density for integrated electron density fluctuations.

The corresponding phase screen autocorrelation functions may be analytically obtained as:

$$B_{\phi}^{(1)}(\xi) = \frac{\xi}{L_0} K_1(\xi/L_0) \quad (1-3)$$

$$B_{\phi}^{(2)}(\xi) = \left(\frac{1}{1+\xi^2/L_0^2} \right) \quad (1-4)$$

 Satellite
Transmitter

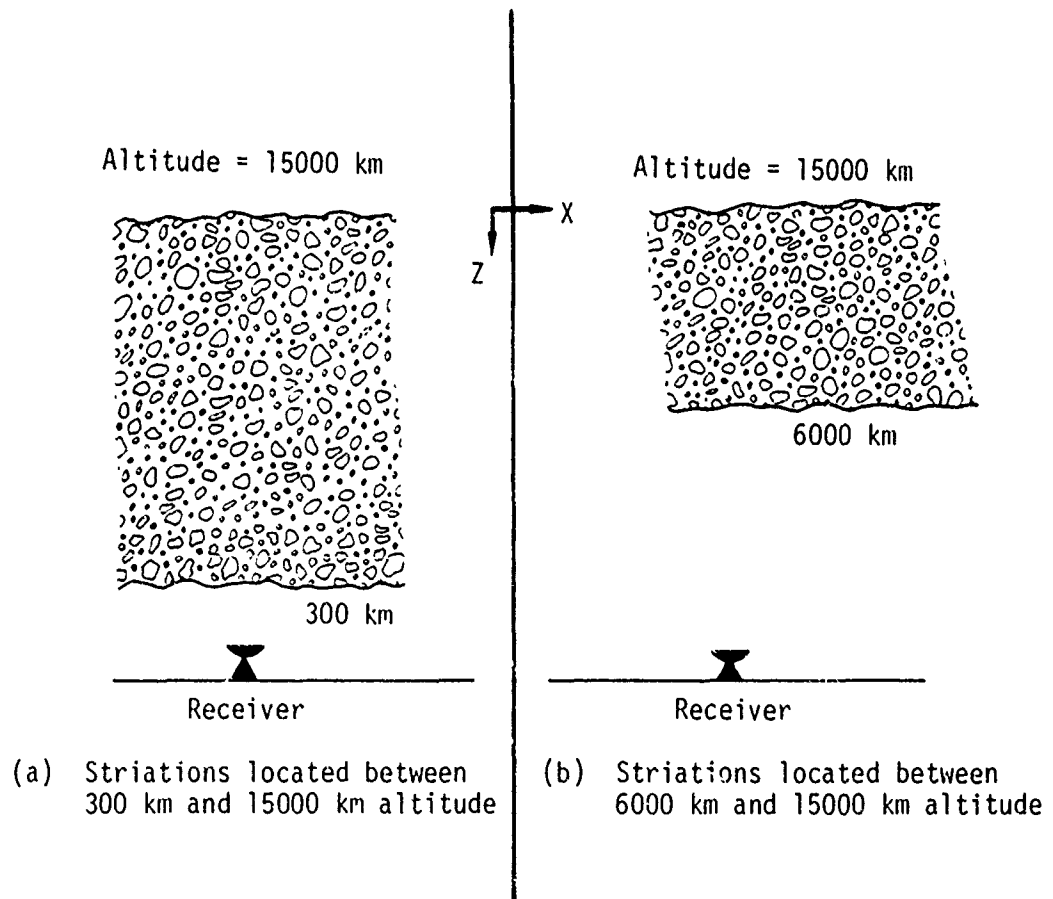


Figure 1. Geometry of DSCS simulation.

where $K_1(x)$ is the modified Bessel function (Abramowitz and Stegun, p. 374). (The Fourier transform relationship used here between autocorrelation function and power spectral density is given by Equations B-11 and B-14.) For this report an important parameter of interest is the autocorrelation length which is defined as the e^{-1} point of the autocorrelation function. For the power law spectrum, $\phi_{\phi}^{(1)}$, the correlation length is $\ell_c^{(1)} = 1.55 L_0$, and for the exponential spectrum, $\phi_{\phi}^{(2)}$, the correlation length is given by $\ell_c^{(2)} = 1.31 L_0$. For this report, the correlation length ranged from 1 to 10 kilometers for both choices of the phase-screen power spectral density.

The final physical parameter of interest is the total phase standard deviation of the phase-screens comprising the multiple phase-screen. Since each phase-screen is designed as an assembly of Gaussian random variables with zero mean and variance $\sigma_{\phi_i}^2$ and is independent of the other individual phase-screens, the total variance is the sum of the individual variances and thus the phase standard deviation is given by

$$\sigma_{\phi} = \left\{ \sum_{i=1}^N \sigma_{\phi_i}^2 \right\}^{1/2} \quad (1-5)$$

where N is the total number of phase-screens. For this work N was chosen to be 10 and σ_{ϕ} ranged from 1.0 to 100 radians.

The main body of this report is divided into three major sections. Sections 2 and 3 show the application of the MPS code to problems whose analytic solutions are available and allow a comparison of the code results to analytical results. Section 2 deals with the calculation of the diffraction pattern of a single Gaussian lens in the center of a phase screen. The analytic solution is obtained as a Fresnel-Kirchhoff integral which may be written as an infinite series and summed. Section 3 shows the results for a single phase-screen characterized by a Gaussian power spectral density

and small phase variance σ_ϕ^2 . Results for the observed intensity power spectral density, and scintillation index are compared with analytic calculations in the weak-scatter approximation. Section 4 describes the results of the DSCS simulation at a frequency of 7.5 GHz. Appendix A contains a description of the multiple phase-screen code, its analytical foundation and the technique used to generate the random phase-screens. Appendix B contains a derivation of the relationship between the phase-screen standard deviation σ_ϕ and the electron density fluctuations and a brief discussion of the relationship between one, two and three-dimensional power spectra. Appendix C shows one realization of all ten phase-screens and traces the signal intensity as the wave propagates through the medium for a particular geometry relevant to DSCS.

SECTION 2

2.0 DIFFRACTION BY A GAUSSIAN LENS

2.1 Gaussian Lens - Code Calculation

As a test of the multiple phase-screen propagation code, a single Gaussian phase lens given by

$$\phi(x) = \phi_0 \exp(-x^2/r_0^2) \quad (2-1)$$

was used at the first phase-screen location ($z = 0.0$) with ϕ_0 chosen as 10 radians and r_0 taken as λ .

The intensity $I = |E|^2$ was observed as a function of distance from the lens, z/λ as indicated in Figure 2(a-b). In this figure, all the phase-screens and observation screens are aligned, so that features of the diffraction pattern can be easily followed for changing z/λ values.

The focal length for a Gaussian lens is given by Salpeter (1967) as $kr_0^2/2\phi_0$ where k is the wavenumber $2\pi/\lambda$. Taking $r_0 = \lambda$ and $\phi_0 = 10$ radians, the focal length F/λ is 0.31 which corresponds reasonably well with the value of $z/\lambda = 0.5$ where the intensity in the diffraction pattern at $x = 0$ builds up to a maximum. At values of z/λ greater than the focal length, the diffraction pattern exhibits increasingly more complex patterns associated with rays coming from the edges of the lens, rather than from the center.

2.2 Gaussian Lens - Analytic Results

An analytical relationship between the electric field at $z = z_1$ and $z = z_2$ is given by the Fresnel-Kirchhoff integral (Ratcliffe, 1956)

$$E(x, z_2) = \left(\frac{i2\pi(z_2 - z_1)}{k} \right)^{-1/2} \int_{-\infty}^{\infty} d\xi e^{-ik(z_2 - z_1)} \times \exp \left\{ i \frac{1}{2} k(x - \xi)^2 / (z_2 - z_1) \right\} E(\xi, z_1) \quad (2-2)$$

where $E(x, z_1)$ is the electric field as a function of x in the $z = z_1$ plane. For an initial electric field in the $z = 0$ plane given by $E(\xi) = \exp i \{ \phi_0 \exp(-\xi^2/r_0^2) \}$, Equation 2-2 may be written as an infinite series by expanding $\exp i \{ \phi_0 \exp(-\xi^2/r_0^2) \}$ in a Taylor series as

$$e^x = \sum_{n=0}^{\infty} \frac{x^n}{n!} \quad (2-3)$$

The resulting integral over ξ may then be analytically performed using Equation 3.323(2) on page 307 of Gradshteyn and Ryzhik (1965). The result may be expressed as

$$E(x', z') = \sqrt{\pi} \frac{e^{i2\pi z'}}{\sqrt{i z'}} e^{i\pi x'^2/z'} \sum_{n=0}^{\infty} \frac{(i\phi_0)^n}{n!} (n/r_0'^2 - i\pi/z')^{-1/2} \exp \left[\frac{-\pi^2 x'^2/z'^2}{(n/r_0'^2 - i\pi/z')} \right] \quad (2-4)$$

where the primed quantities $x' = x/\lambda$, $z' = z/\lambda$, and $r_0' = r_0/\lambda$. This series is easily summed (numerically) and the results for several values of z/λ are shown in Figure 2 to be identical to the code calculation for $z/\lambda \leq 2.0$.

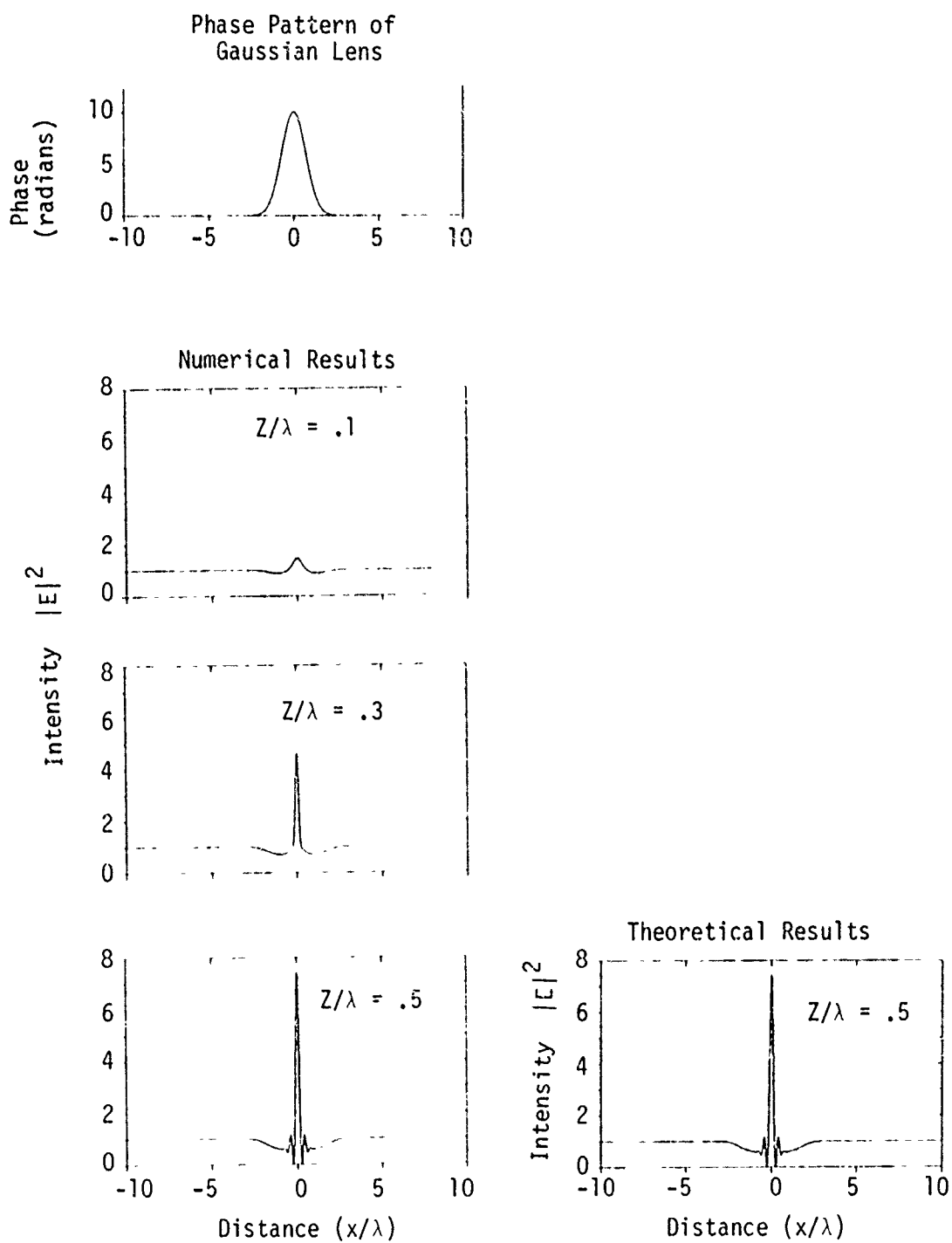


Figure 2(a). Diffraction pattern of a Gaussian lens - numerical results from simulation on left-hand side versus theoretical results on right-hand side.

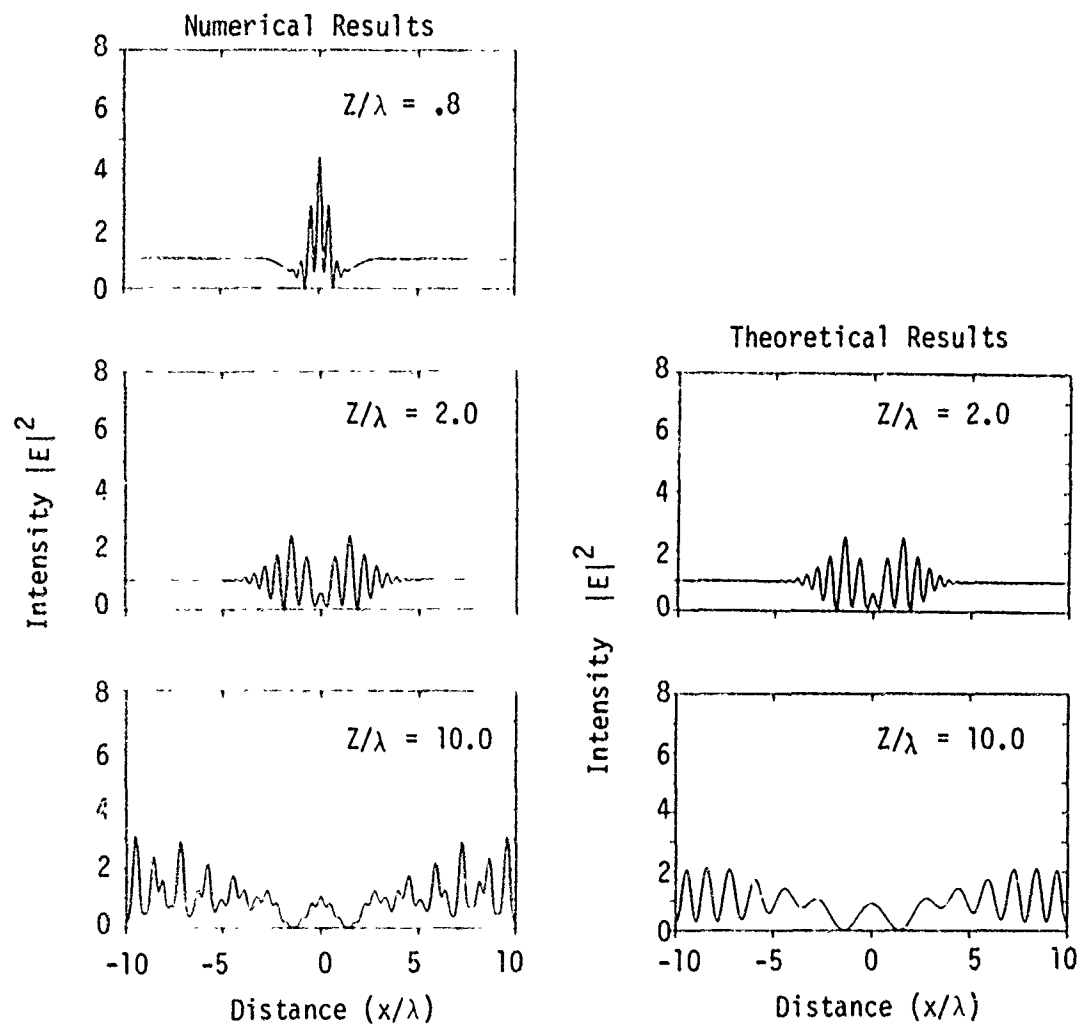


Figure 2(b). Diffraction pattern of a Gaussian lens - numerical results from simulation on left-hand side versus theoretical results on right-hand side.

For $z/\lambda = 10$ the multiple phase-screen calculations deviate from the theoretical results because energy which has left one side of the grid is coming back into the other side (this is the well known wrap-around or aliasing effect in fast Fourier transforms). Hendrick (1977) has determined criteria required to avoid this and other numerical problems and these criteria were used to assure proper application of the code results.

SECTION 3

3.0 DIFFRACTION BY A RANDOM THIN PHASE-SCREEN

This section contains a second application of the multiple phase-screen propagation code to a problem for which analytical results are available - scattering through a thin phase-screen characterized by a Gaussian power spectral density. For this example, only one phase-screen was used to characterize the random medium. The screen was located at $z = 0$ and was generated with a phase power spectral density (PSD) of

$$\Phi_{\phi}(K) = \sigma_{\phi}^2 \frac{x_0}{2\sqrt{\pi}} \exp(-K^2 x_0^2/4) \quad (3-1)$$

where the phase standard deviation was chosen as $\sigma_{\phi} = 0.1$ radians and x_0 was taken as 1λ . The corresponding phase autocorrelation function is then

$$B_{\phi}(\xi) = \exp(-\xi^2/x_0^2) \quad (3-2)$$

To obtain statistical results for the received signal, the simulation was exercised ten times with ten different random phase-screens (each screen chosen used a different set of random numbers; see Appendix A). Figure 3 shows a comparison of the intended phase-screen power spectral density $\Phi_{\phi}(K')$ where $K' = K\lambda$ (dotted line) with the actual mean power spectral density obtained by averaging the power spectral densities of each of the ten realizations. Although no statistical study was performed to show the effect of averaging over different numbers of realizations this result indicates that ten realizations are sufficient to obtain reasonably accurate statistics.

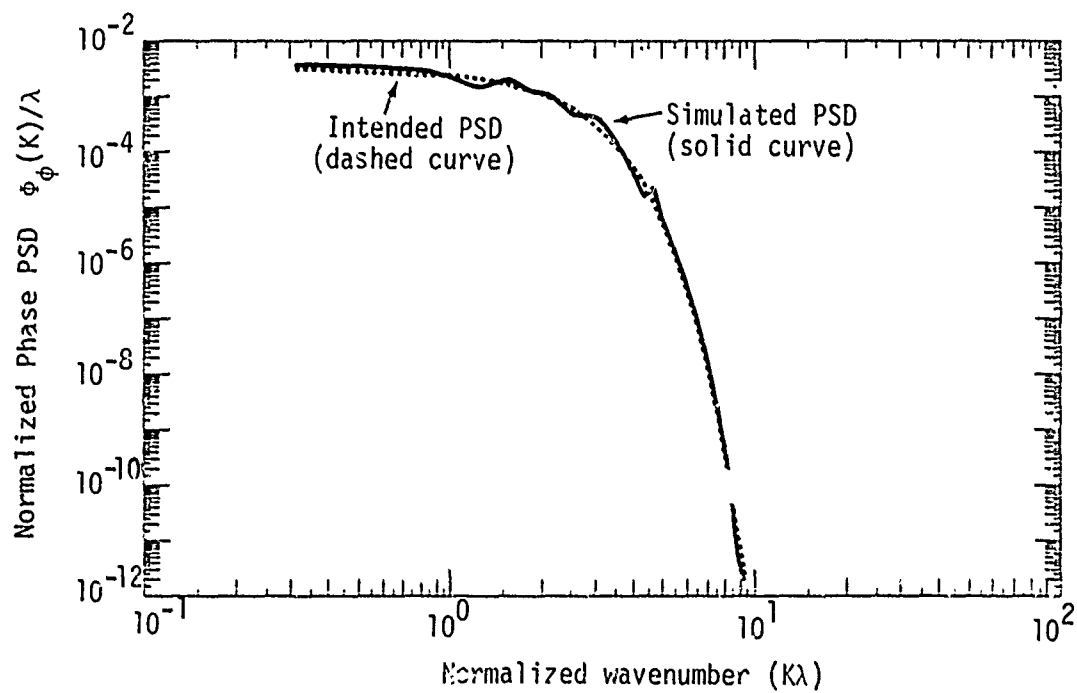


Figure 3. Comparison of intended phase-screen power spectral density with that generated by the simulation for $\sigma_{\phi_i} = 0.1$ radians.

Figure 4 shows the average intensity $\langle |E|^2 \rangle$ power spectral density at the locations $z/\lambda = 0.628, 6.28, \text{ and } 37.7$, each compared to the theoretical results from Salpeter (1967)

$$\Phi_I(K) = 4\Phi_\phi(K) \sin^2(K^2 z/2k). \quad (3-3)$$

(Strictly speaking Φ_I is the PSD of the normalized intensity deviation $(|E|^2 - \langle |E|^2 \rangle) / \langle |E|^2 \rangle$). Excellent agreement between the theoretical and simulation results is shown with the simulation results for $z/\lambda = 6.28$ even matching the location of the nulls (but not the infinite depth) of the analytical result. In all three curves the simulation deviates from the analytical results for large wavenumbers, which is likely caused by aliasing which always occurs in the application of fast Fourier transform techniques. A second possible explanation for this deviation at large wavenumbers is that the small scale sizes may produce angular scatter which causes this portion of the wave to alias to the other side of the phase screen. However, this aliasing behavior should become more pronounced as the propagation distance z/λ increases. Since this is not the case for Figure 4, this explanation must be discarded. For $z/\lambda = 37.7$ the simulation accurately models the peaks of the analytical curve. However, except for the first null at $K\lambda \approx 1$ ($K^2 z/2k = \pi$), the details of the nulls are lacking. This smearing of the nulls is caused by the averaging process.

The circled dots of Figure 5 show the value of scintillation index S_4 obtained from the simulation for values of σ_ϕ of 0.1, 1.0 and 10.0 radians. The solid curves are analytical estimates taken from the weak-scatter approximation of Salpeter

$$S_4^2 = 4 \int_{-\infty}^{\infty} \Phi_\phi(K) \sin^2 \left[\frac{K^2 z}{2k} \right] dK \quad (3-4)$$

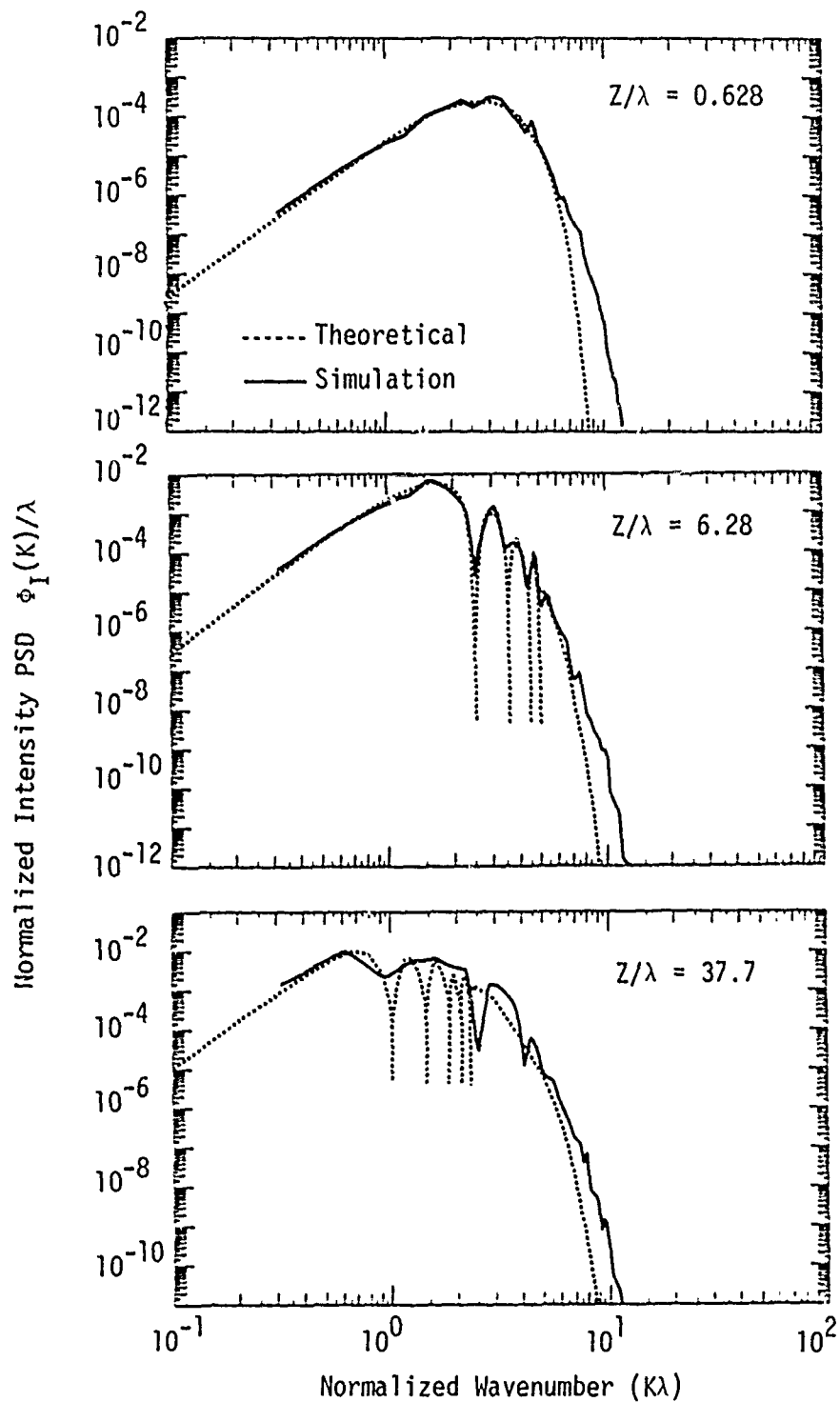


Figure 4. Normalized intensity PSD as a function of distance from a thin, Gaussian phase-screen ($\sigma_\phi = 0.1$ radians, $x_0 = \lambda$).

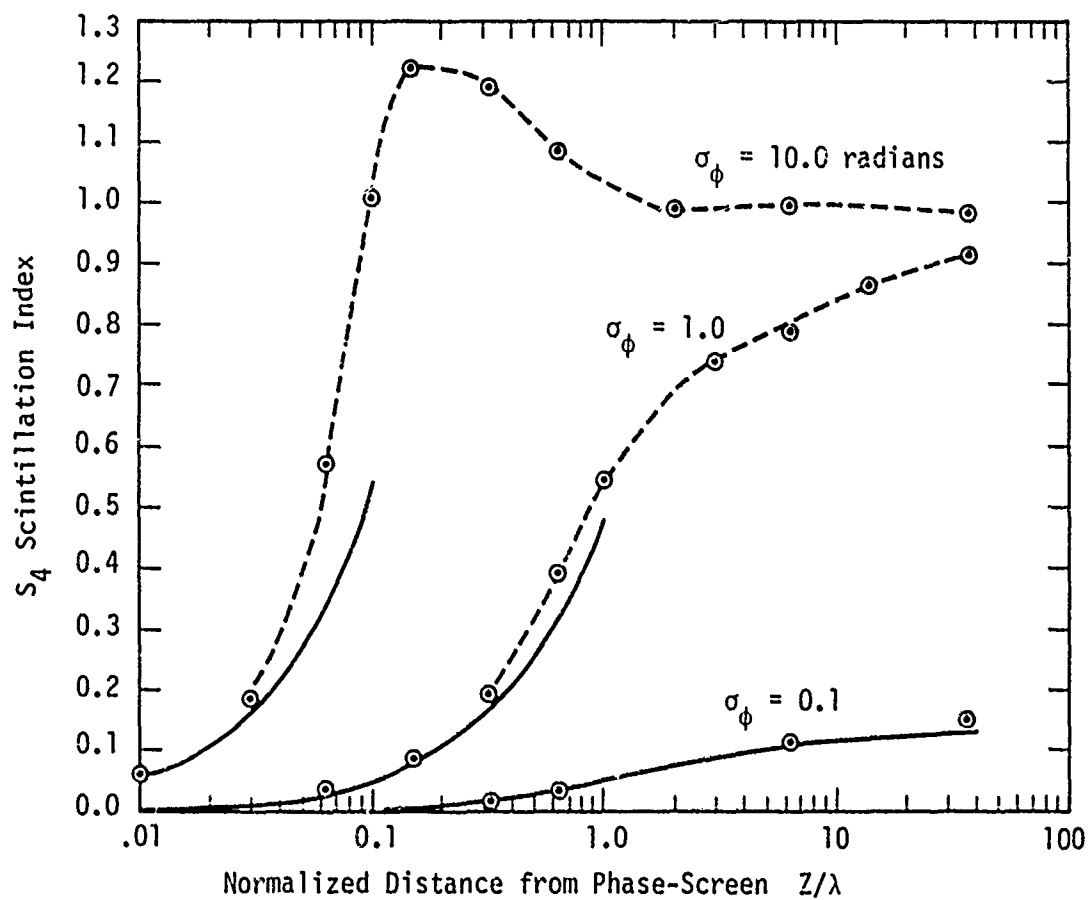


Figure 5. Circled dots show S_4 scintillation index for Gaussian spectrum. The solid lines are analytic approximations valid for the weak-scatter case ($x_0 = \lambda$).

which may be exactly integrated for the Gaussian phase power spectral density given by Equation (3-1) to obtain

$$S_4^2 = \sigma_\phi^2 \left\{ 2 - \left(\frac{1}{16} + \frac{z^2}{k^2 x_0^4} \right)^{-1/4} \cos \left(\frac{1}{2} \tan^{-1} \frac{4z}{k x_0^2} \right) \right\} . \quad (3-5)$$

It is seen from Figure 5 that excellent agreement is obtained between this analytical approximation and simulation results when the weak-scatter assumption inherent in Equation 3-5 is valid.

SECTION 4

4.0 DSCS SIMULATION RESULTS

This section describes the results of the simulation as applied to the satellite communication problem discussed in the introduction. As stated there, the simulation was applied to the two geometries shown in Figure 1, for two different phase-screen PSD's as given by Equations 1-1 and 1-2. The phase correlation lengths ranged from 1 to 10 km, and the phase standard deviation (as given by Equation 1-5) ranged from 1.0 to 100 radians. Table 4-1(a) and (b) shows the cases which were simulated for the power-law PSD and for the exponential PSD respectively. In addition to the phase correlation length, ℓ_c , and phase standard deviation, σ_ϕ , for each case the simulated phase-screen length L is also included. In all cases, for this section of the report, the statistical results were obtained by averaging results for ten different realizations of the problem. For each realization, the striated region was represented by ten phase-screens, each composed of 2048 points.

In general, the results were not a strong function of the two geometries shown in Figure 1. For the weak scattering cases listed in Table 4, the scintillation index for the thicker striation region geometry (Figure 1(a)) was up to 25% less than that for the thinner region with the same total phase standard deviation. This is intuitively expected since for the thicker geometry, the phase-screens very close to the receiver plane will not be as effective at producing amplitude scintillation as phase-screens farther away. In the rest of this section only results for the geometry of Figure 1(a) are presented.

Table 4-1(a). Simulation parameters for power-law PSD.

Phase Correlation Length ℓ_c	Phase Standard Deviation σ_ϕ	Phase Screen Length L	Resulting Scintillation Index	
			Geometry 1*	Geometry 2**
1 km	1.0 rad	30 km	.37	.42
1	2.5	30	.83	.85
1	3.16	30	.94	.93
1	10.0	30	1.05	.98
3	3.16	50	.41	.48
3	10.0	50	1.03	1.06
10	10.0	100	.41	.49
10	31.6	100	1.05	1.05

Table 4-1(b). Simulation parameters for exponential PSD.

Phase Correlation Length ℓ_c	Phase Standard Deviation σ_ϕ	Phase Screen Length L	Resulting Scintillation Index	
			Geometry 1*	Geometry 2**
1 km	1.0 rad	30 km	.32	.39
1	2.5	30	.79	.87
1	3.16	30	.93	.96
1	10.0	30	1.15	1.04
3	3.16	50	.16	.20
3	10.0	50	.67	.89
3	31.6	50	1.60	1.48
10	10.0	100	.05	.06
10	31.6	100	.15	.19
10	50.0	100	.25	.34
10	100.0	100	.89	1.15

* Geometry 1 refers to Figure 1(a)

** Geometry 2 refers to Figure 1(b).

In Figure 6 the scintillation index is shown as a function of the total integrated phase standard deviation σ_ϕ for both spectra for values of the striation autocorrelation distance of 1, 3 and 10 kilometers. As expected, the scintillation index increases with increasing σ_ϕ but should ultimately saturate at a value of unity, characteristic of Rayleigh electric field strength statistics (Fante, 1977). Values greater than unity prior to saturation are not prohibited and have been observed in ionospheric measurements (Dr. E.J. Fremouw, personal communication, Stanford Research Institute, 1977). The large value of 1.6 for S_4 in Figure 6 is caused by strong focussing effects.

Figure 7 shows results obtained for the autocorrelation distance of the signal intensity as a function of the total phase standard deviation for the same cases as shown in Figure 6. These results were obtained by finding the distance corresponding to the e^{-1} point from the circular correlation functions obtained from the average of the ten realizations. The general trend of decreasing correlation distance with increasing σ_ϕ is expected intuitively as is the association of large autocorrelation length with large striation autocorrelation distance. The range of these curves is limited by requirements on the phase-screen sampling distances. In order to extend the calculation of the intensity correlation distance farther into the multiple-scatter regime two techniques appear useful. The first involves a numerical solution of the differential equations for the mutual coherence function $\langle I(\rho) I(\rho+\xi) \rangle$ as discussed by Yeh, et al., (1975). A second possible method involves an approximate theory developed by Fante (1975). Both techniques require further evaluation.

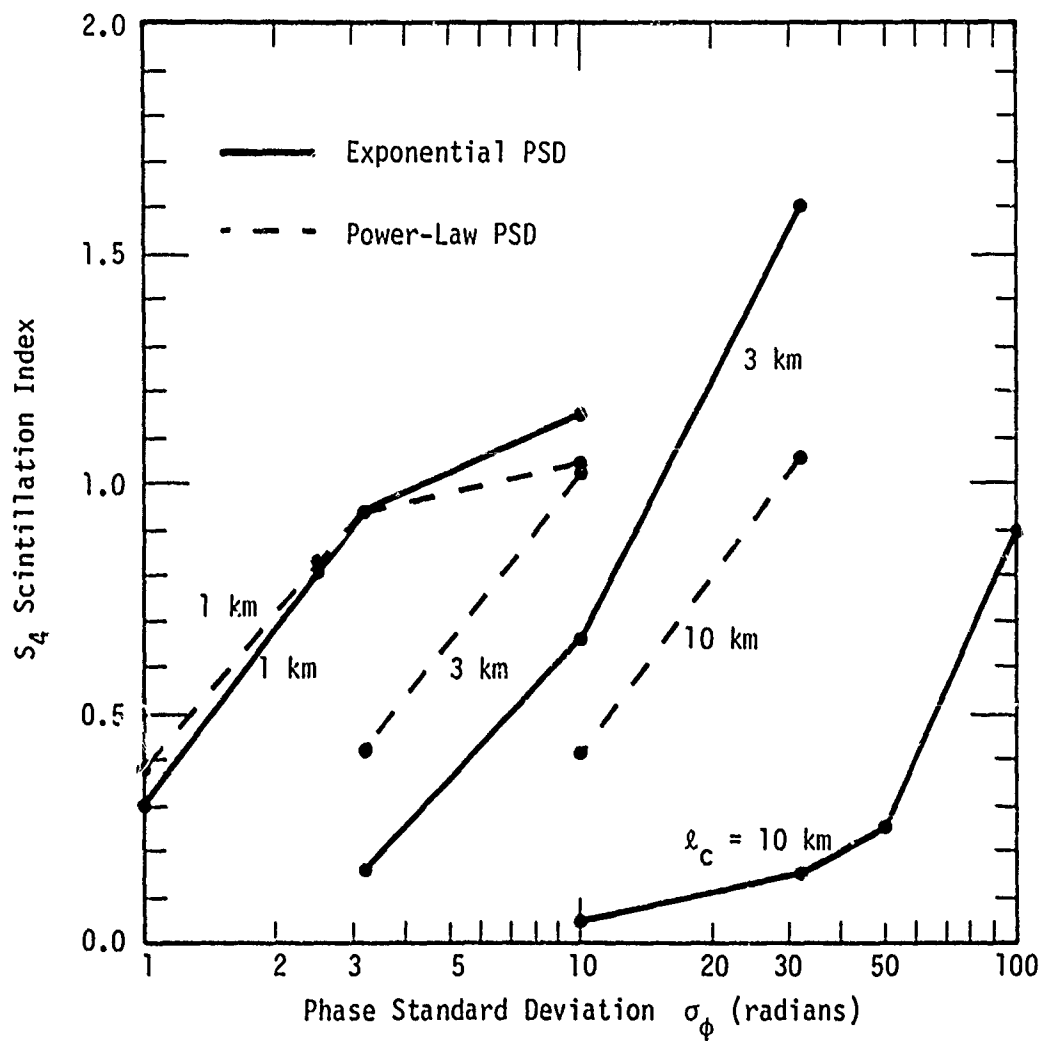


Figure 6. S_4 scintillation index versus σ_ϕ as a function of phase-screen PSD and correlation length l_c for $l_c = 1, 3$, and 10 km.

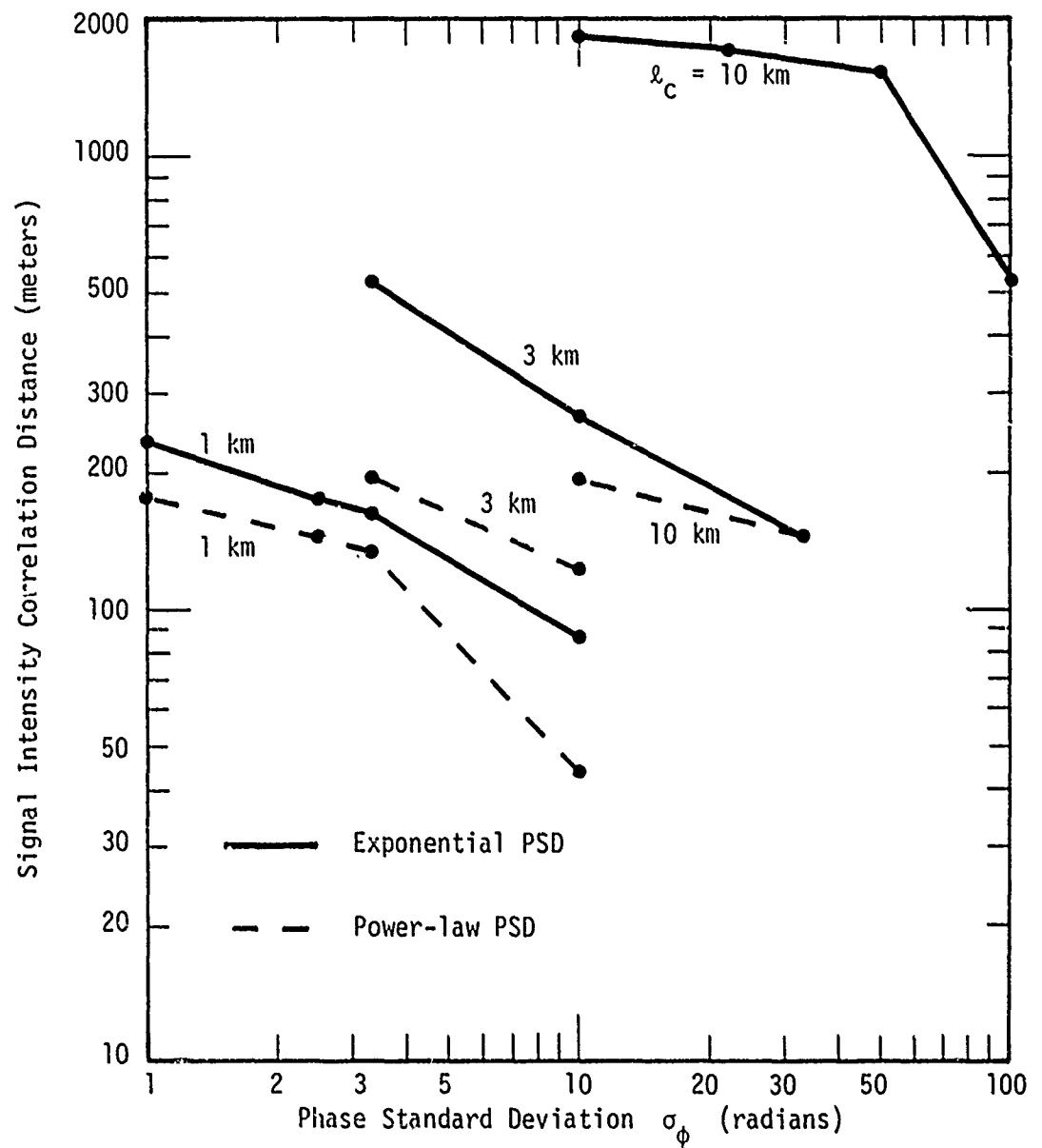


Figure 7. Signal intensity correlation distance versus σ_ϕ as a function of phase-screen PSD and correlation length ℓ_c for $\ell_c = 1, 3$, and 10 km.

4.1 Simulation Results - 1 kilometer Correlation Length

This section and the following two sections discuss the results obtained for realizations of the DSCS propagation simulation. In all cases the random number seed was the same for each computer run so that the set of phase-screen realizations was similar in "overall" appearance for all the runs. This also has the result that some features of the received intensity and phase are recognizable as the phase standard deviation and correlation length change.

Figure 8 shows a comparison of the actual power spectral densities of the phase-screens as generated by the MPS simulation for a one kilometer correlation length. Since the Fresnel length $\sqrt{\lambda z}$ ranges from 0.1 km ($z = 300$ km) to 0.8 km ($z = 15000$ km) which correspond to the wavenumber regime from 7.8 km^{-1} to 62.8 km^{-1} , where the spectra are somewhat similar, the overall simulation results should be similar for these two spectra, since amplitude scintillations are caused by irregularities whose scale sizes are of the order of the Fresnel length. But since the power-law spectrum is somewhat higher at high wavenumbers (corresponding to smaller scales), the received electric field should exhibit more small-scale structure for the power-law PSD.

This behavior is evident in Figures 9 and 10 which show one realization of received intensity ($I = |E|^2$) for the two PSD's for values of the phase standard deviation of 1.0, 3.16 and 10.0 radians. Figures 11 and 12 show the phase (plotted between $\pm\pi$) corresponding to the intensities shown in Figures 9 and 10.

Figures 13 and 14 show the intensity power spectral density corresponding to the cases shown in Figures 9 and 10. (The results shown in Figures 13 and 14 result from averaging the PSD's of ten realizations, the

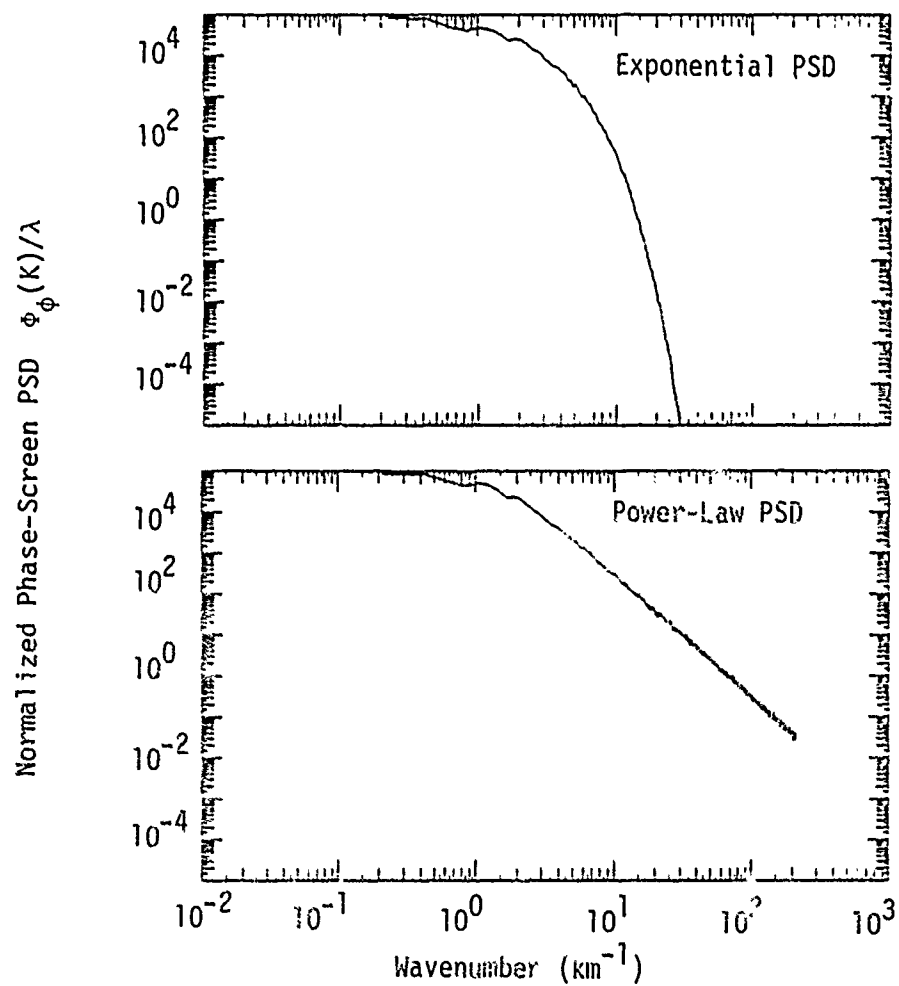


Figure 8. Comparison of simulation generated phase-screen PSD's for correlation length $\ell_c = 1$ km, $\lambda = 0.04$ m. ($\sigma_{\phi_i} = \sqrt{10}$ radians in figure).

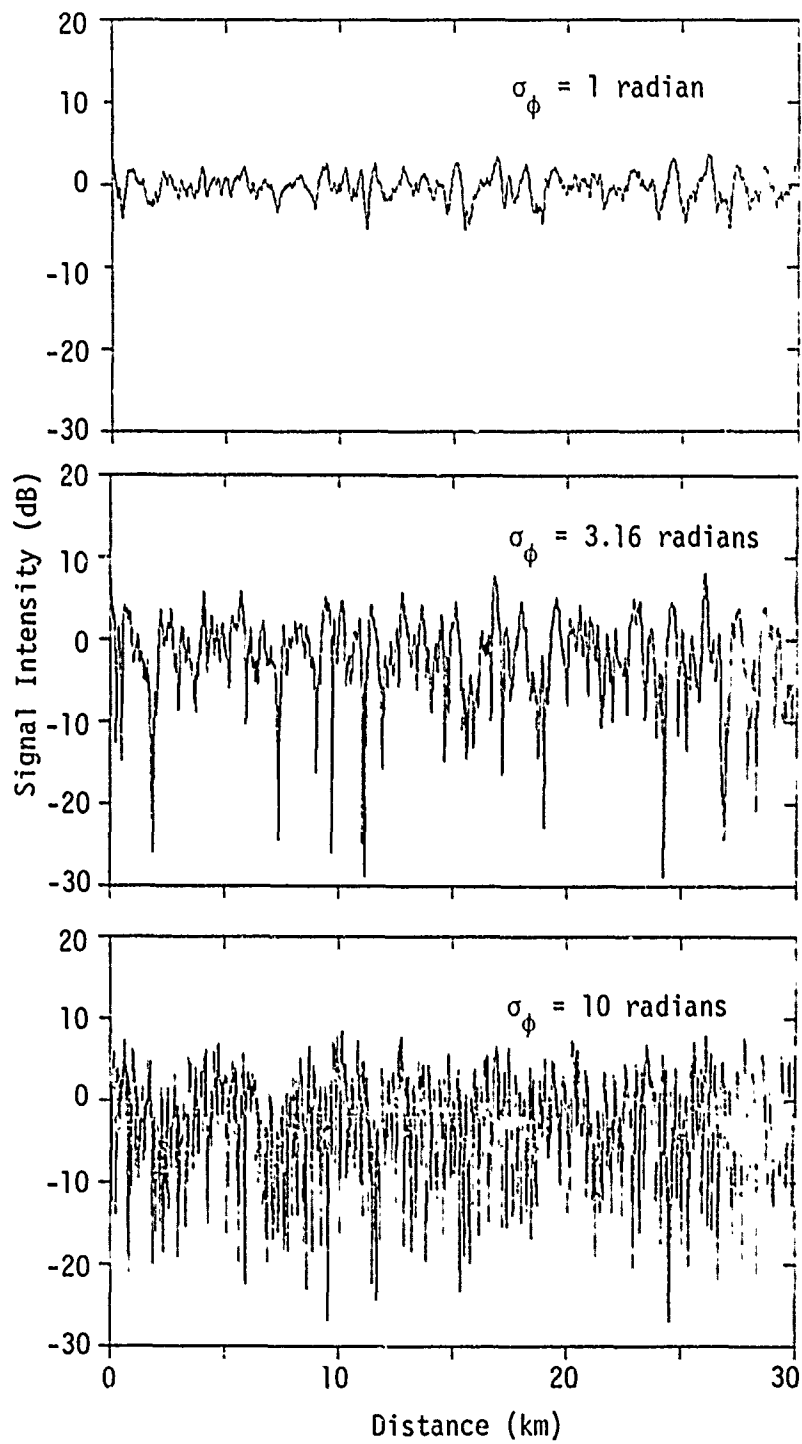


Figure 9. Realizations of signal intensity for power-law PSD with $\lambda_c = 1$ km.

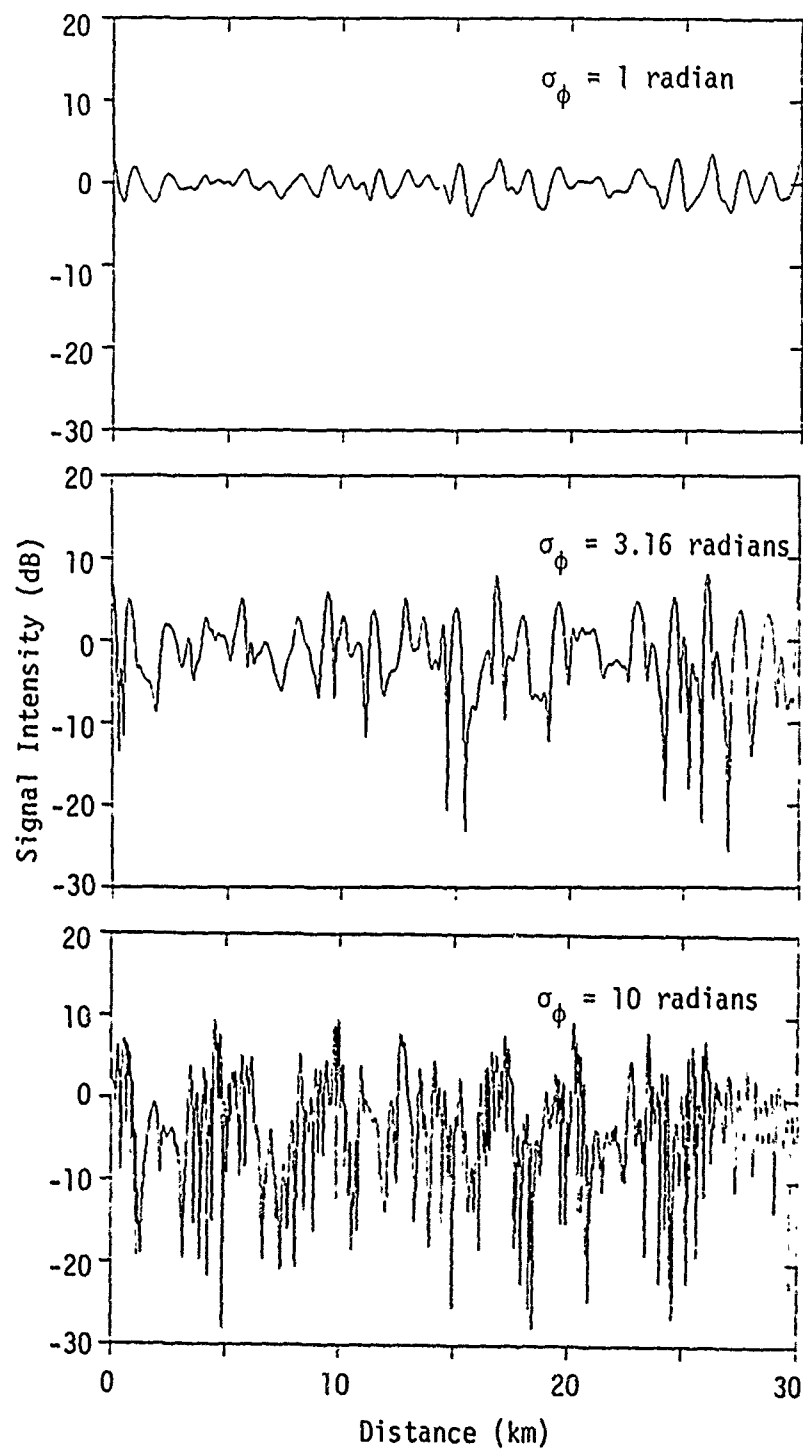


Figure 10. Realizations of signal intensity for exponential PSD with $\lambda_c = 1 \text{ km}$.

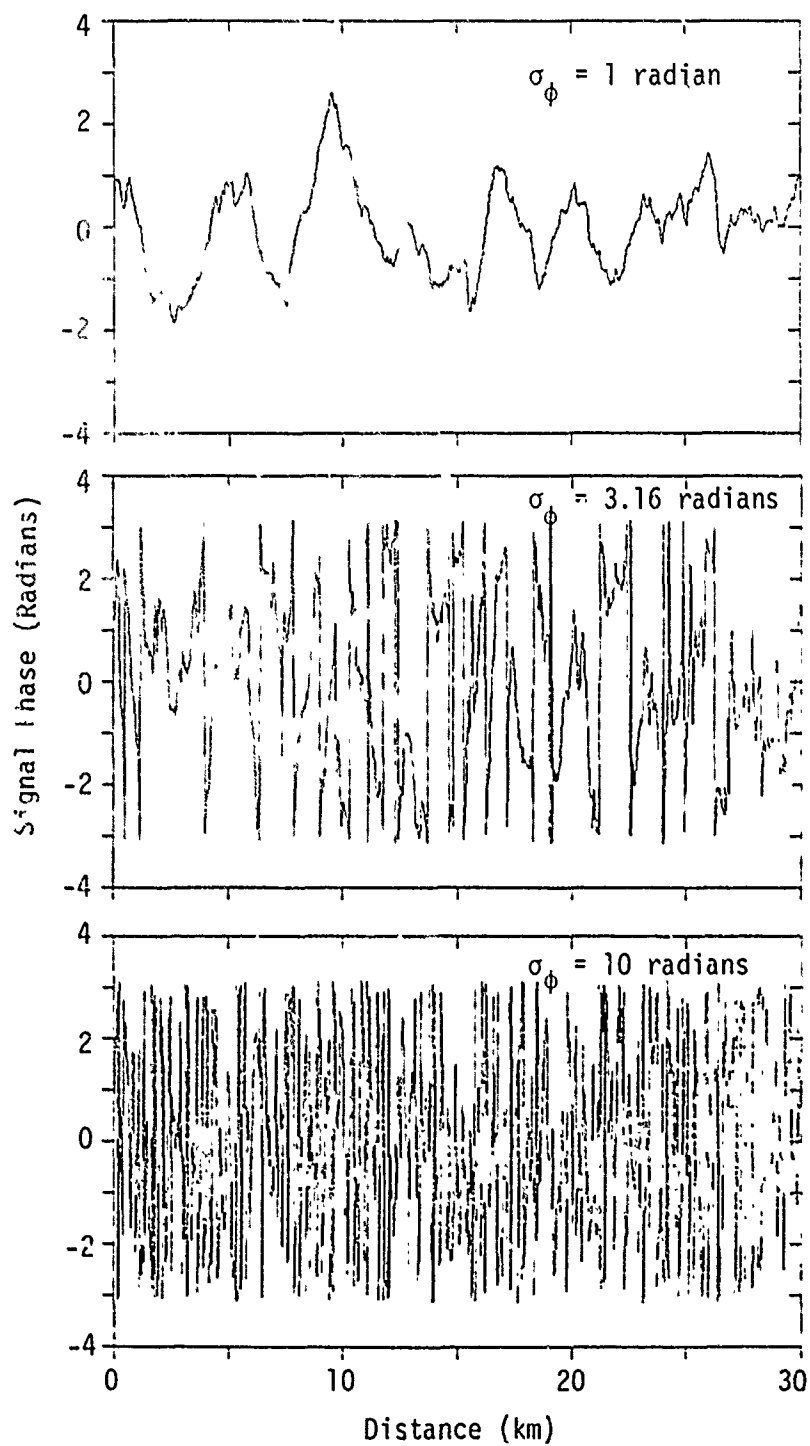


Figure 11. Realizations of signal phase for power-law PSD with $\ell_c = 1 \text{ km}$.

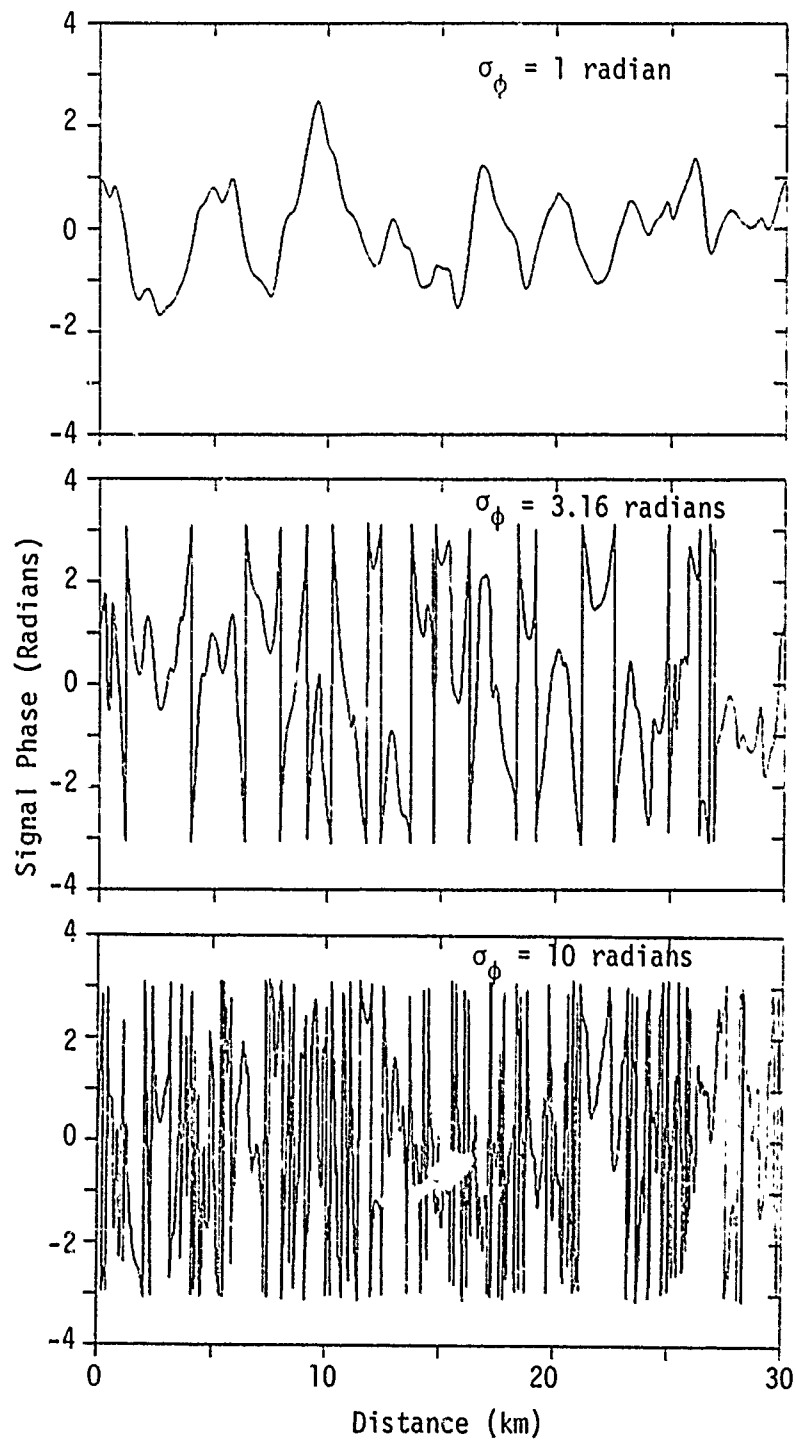


Figure 12. Realizations of signal phase for exponential PSD with $\lambda_c = 1$ km.

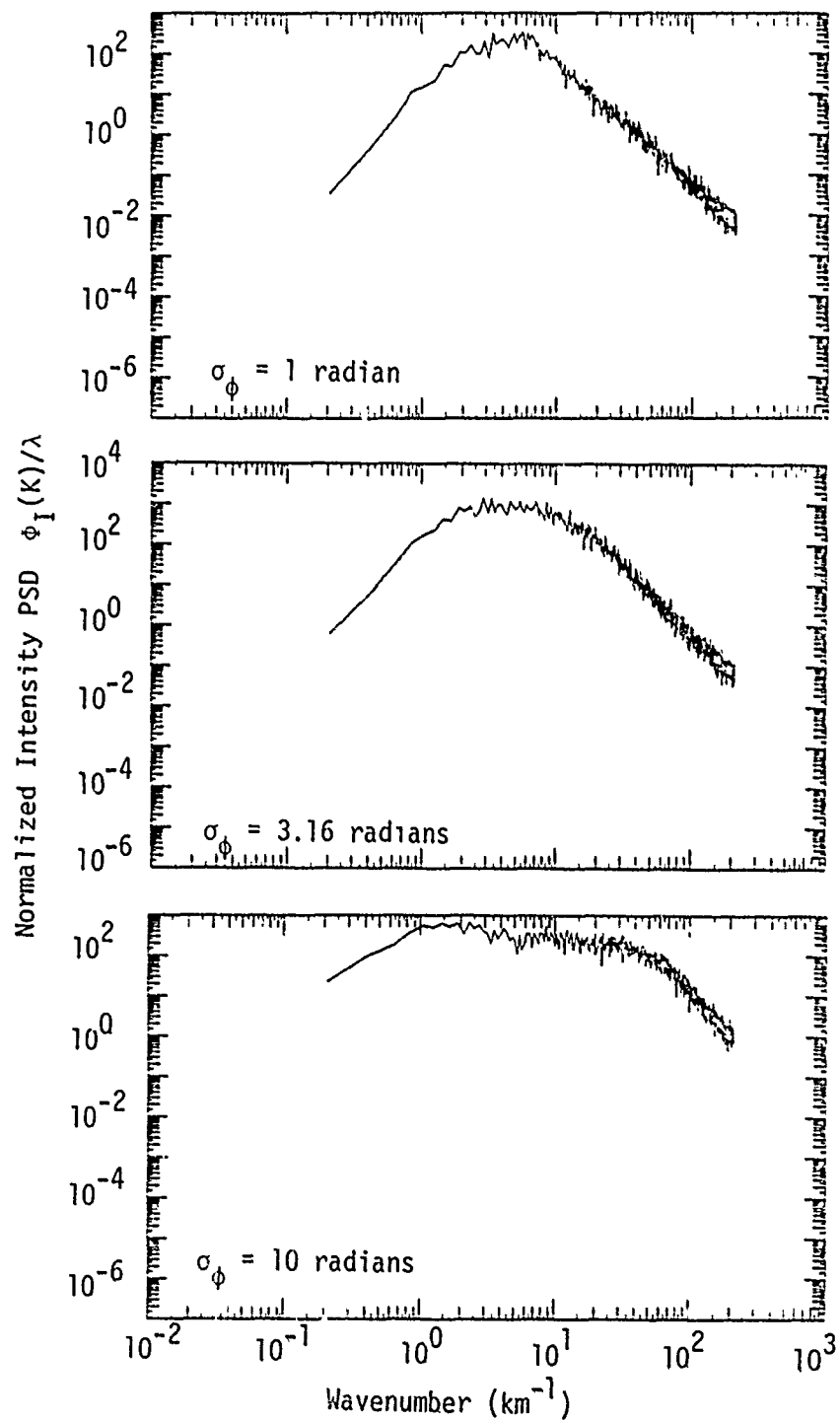


Figure 13. Normalized intensity PSD for power-law phase-screen PSD with $\ell_c = 1 \text{ km}$, $\lambda = 0.04 \text{ m}$.

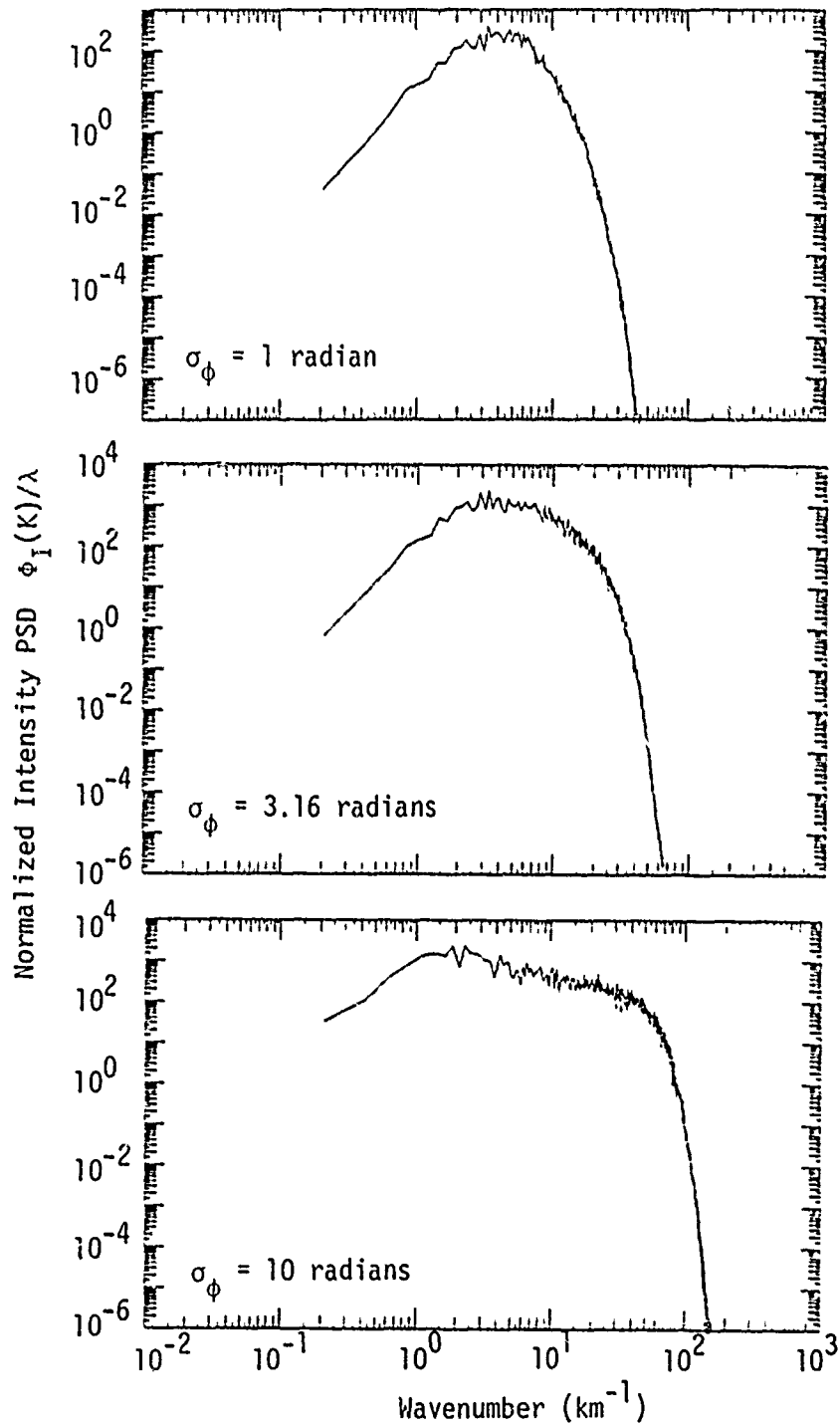


Figure 14. Normalized intensity PSD for exponential phase-screen PSD with $\ell_c = 1$ km, $\lambda = 0.04$ m.

first of which is shown in Figures 9 and 10.) For the weak scattering cases ($\sigma_\phi = 1.0$) the intensity PSD closely matches the PSD of the phase-screen for wavenumbers greater than the inverse Fresnel length. This behavior is required by Equation 3-3 for weak scattering since the intensity PSD is the product of the phase-screen PSD with a sine-squared factor which averages to 1/2 for wavenumbers much greater than the inverse Fresnel length. For the strong scattering cases ($\sigma_\phi > 1.0$), the intensity PSD gradually becomes flatter near the inverse Fresnel length but retains a high-wavenumber roll-off where the spectrum again has the same slope as the phase-screen PSD. This flat low-wavenumber spectrum with a high-wavenumber rolloff is similar to observations of intense ionospheric scintillations shown by Whitney and Basu (1977). This flattening of the intensity PSD, of course, also corresponds to a sharpening of the intensity autocorrelation function with a resulting decrease in the signal intensity correlation distance with increasing σ_ϕ . This behavior is shown in Figure 7.

4.2 Simulation Results - 3 kilometer Correlation Length

Figure 15 shows a comparison of the measured (simulation) phase-screen PSD's for a phase correlation length of 3 km. For this case, the power-law PSD is much larger than the exponential PSD near wavenumbers corresponding to the Fresnel length, and therefore one would expect a much greater difference between the received signals for the $\ell_c = 3$ km case than for the $\ell_c = 1$ km case discussed in the previous section.

The difference is apparent in Figures 16 and 17 which show realizations of the received intensity for values of $\sigma_\phi = 3.16$ and 10.0 radians for the power-law PSD and $\sigma_\phi = 3.16, 10.0$ and 31.6 radians for the exponential PSD. Note the absence of small scale structure for the exponential PSD for $\sigma_\phi = 3.16$ and 10.0 radians.

The phases corresponding to the intensities of Figures 16 and 17 are shown in Figures 18 and 19.

For the interested reader Appendix C shows the realization of the ten phase-screens and the electric field intensity as the wave progresses through the screens to the observation plane for the case $\sigma_\phi = 31.6$ and the exponential PSD.

Figures 20 and 21 show the mean intensity PSD's corresponding to the intensity realizations shown in Figures 16 and 17. Again, as the phase standard deviation σ_ϕ increases, the intensity PSD goes from a close resemblance to the phase-screen PSD for wavenumbers greater than the inverse Fresnel distance to a much flatter behavior for larger σ_ϕ .

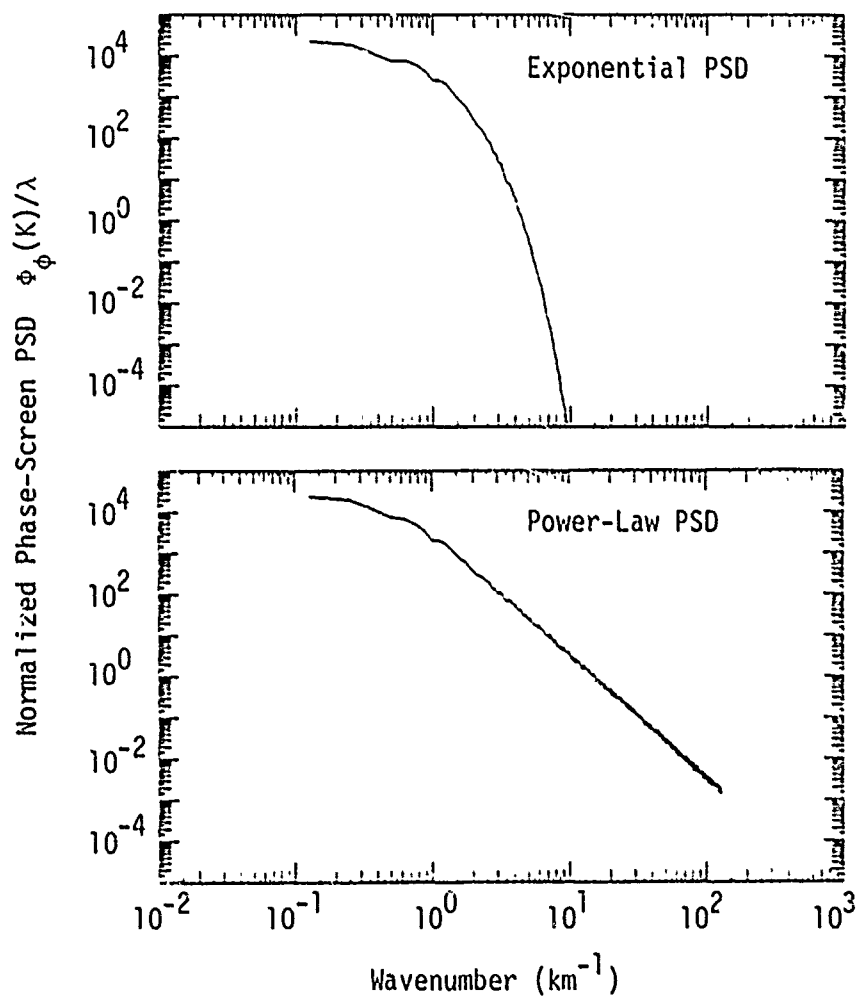


Figure 15. Comparison of simulation generated phase-screen PSD's for correlation length $l_c = 3$ km, $\lambda = 0.04$ m. ($\sigma_{\phi_i} = \sqrt{10}$ radians in figure).

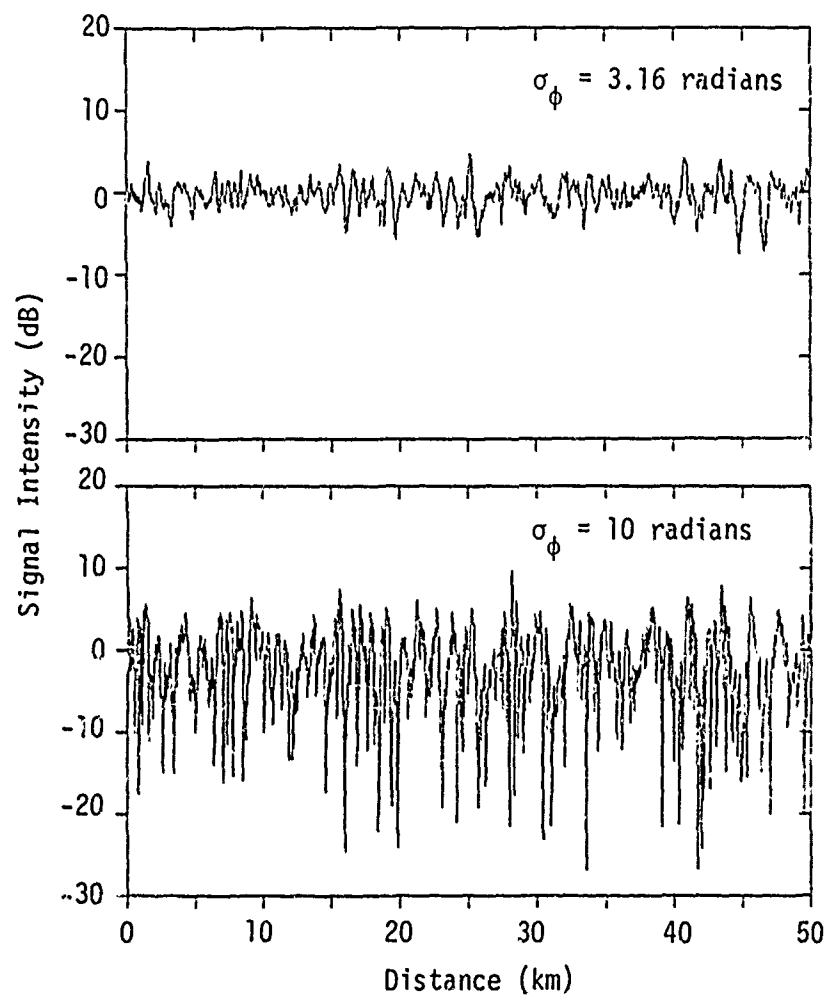


Figure 16. Realizations of signal intensity for power-law PSD with $\lambda_c = 3$ km.

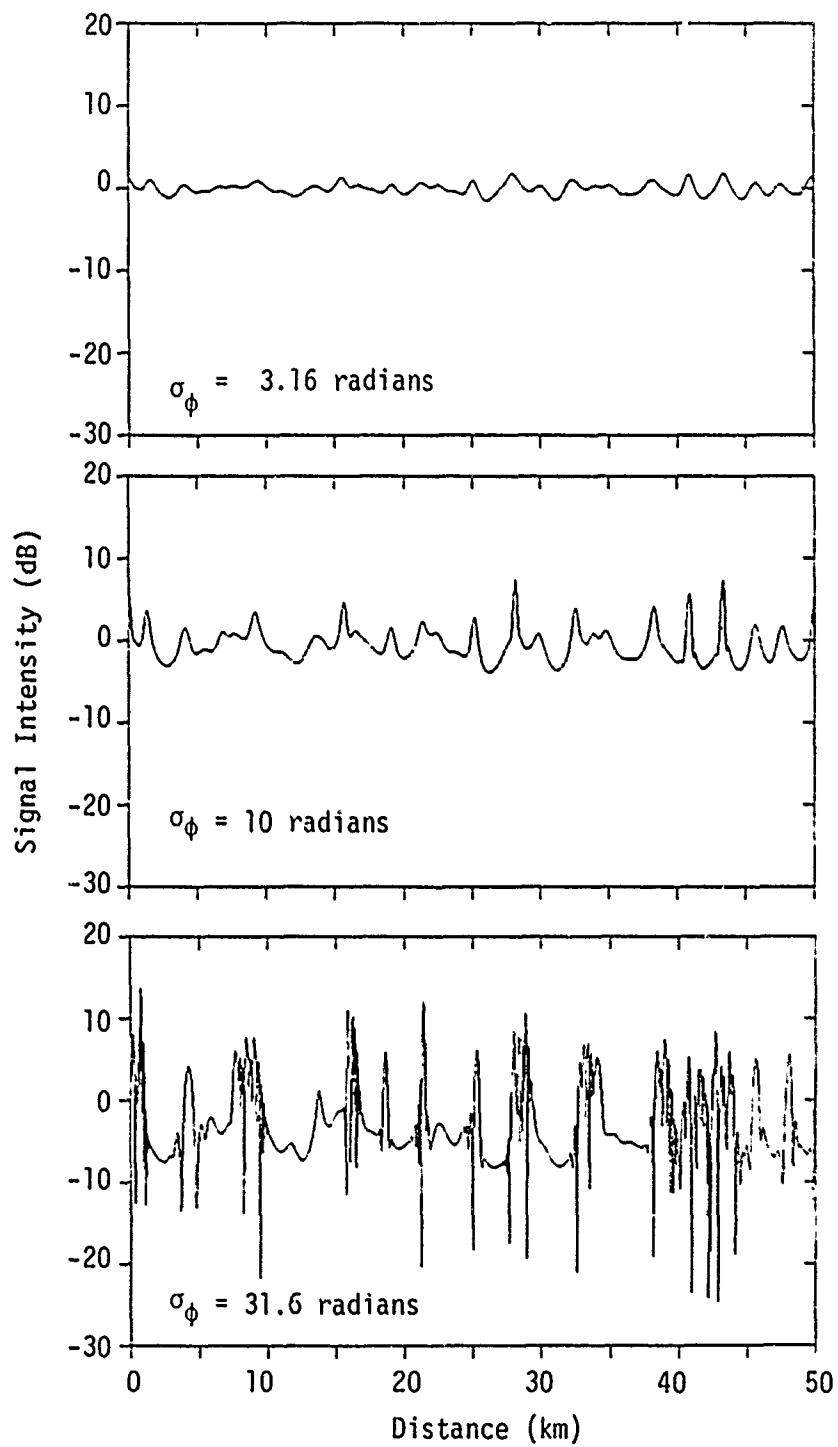


Figure 17. Realizations of signal intensity for exponential PSD with $\ell_c = 3$ km.

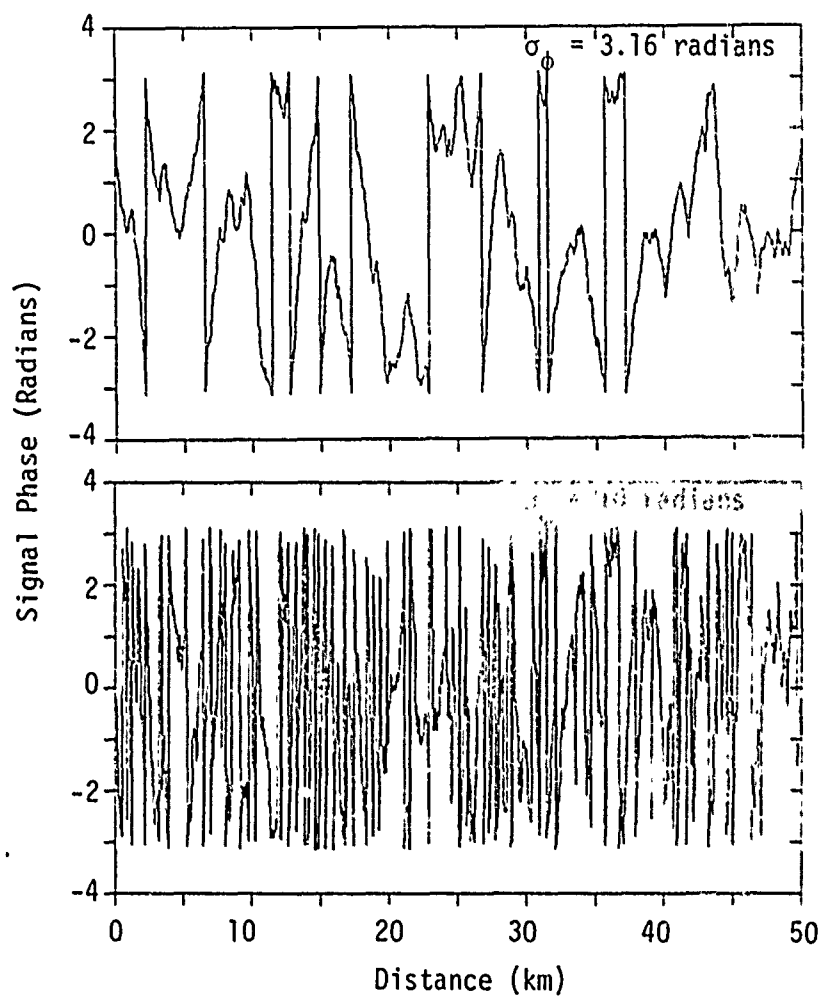


Figure 18. Realizations of signal phase for power-law PSD with $\lambda_c = 3$ km.

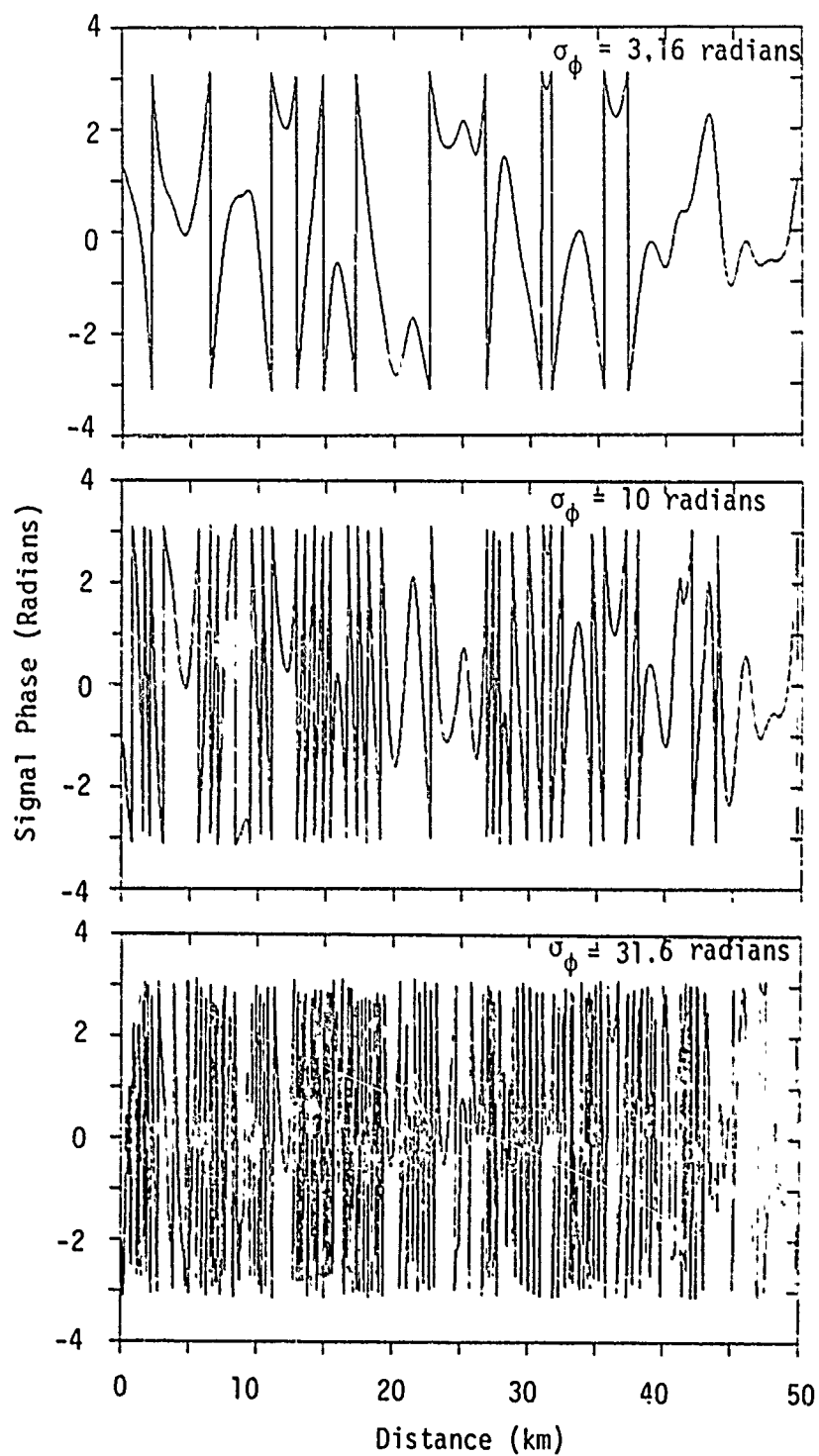


Figure 19. Realizations of signal phase for exponential PSD with $\lambda_c = 3$ km.

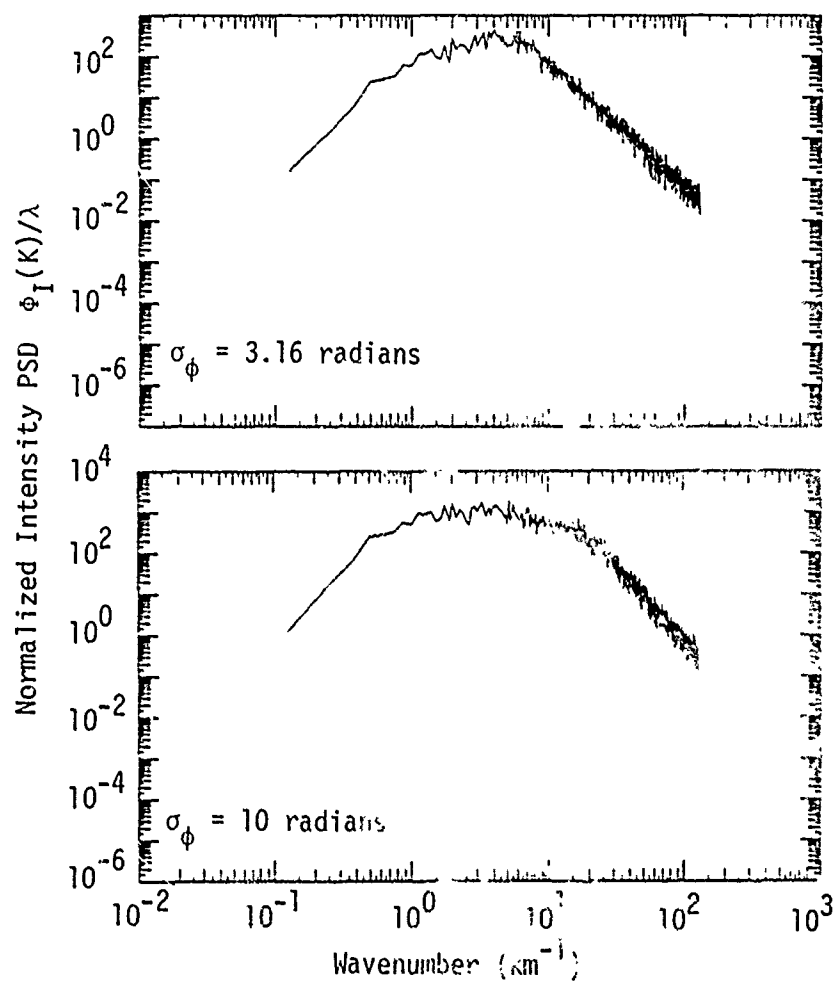


Figure 20. Normalized intensity PSD for power-law phase screen PSD with $\ell_c = 3 \text{ km}$, $\lambda = 0.04 \text{ m}$.

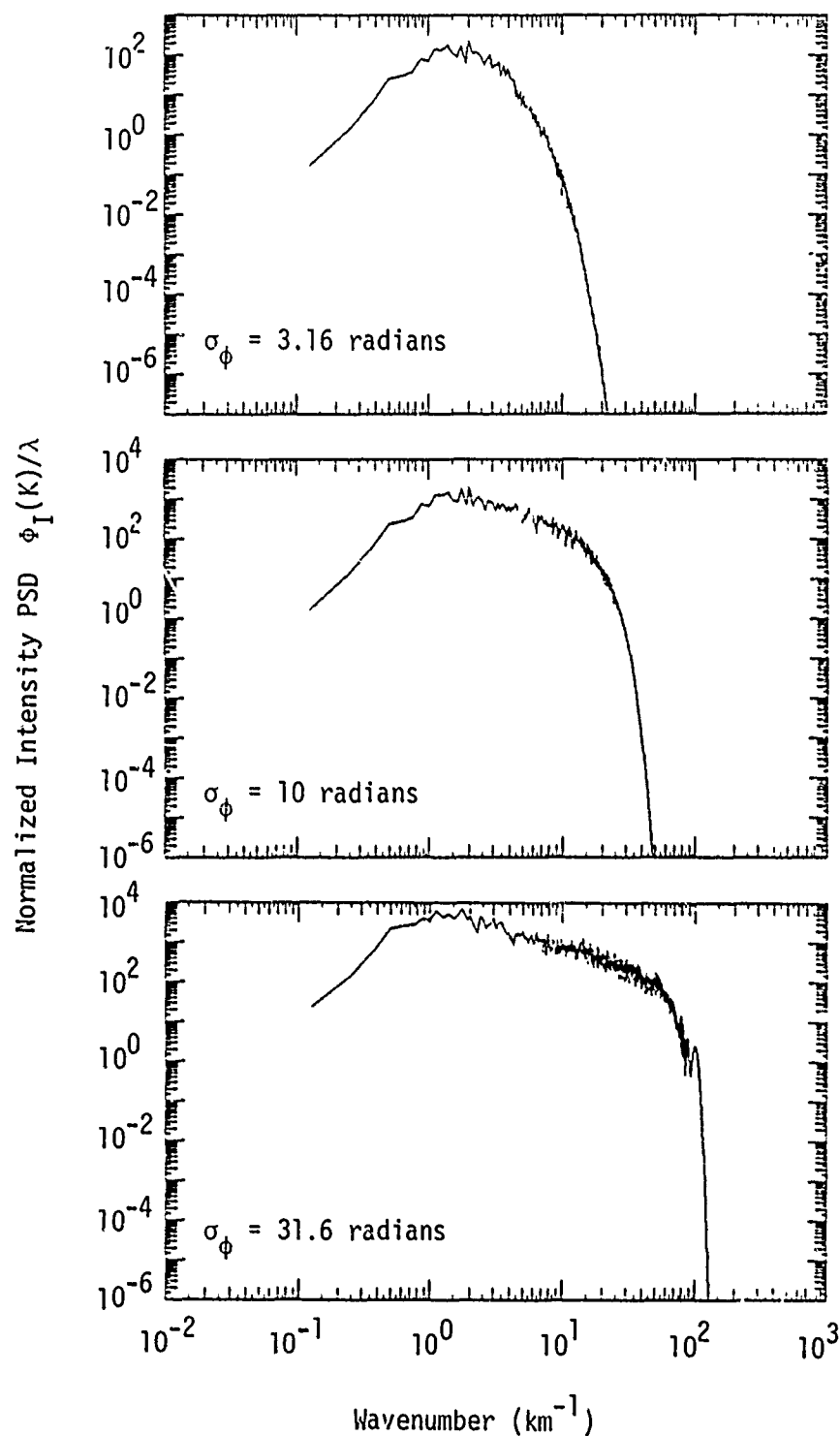


Figure 21. Normalized intensity PSD for exponential phase-screen PSD with $\ell_c = 3 \text{ km}$, $\lambda = 0.04 \text{ m}$.

4.3 Simulation Results - 10 kilometer Correlation Length

For phase correlation length $\ell_c = 10$ km, the two phase-screen PSD's generated by the code differ significantly in the wavenumber region near the inverse Fresnel length as shown in Figure 22. This difference is dramatically shown in Figures 23 and 24 which show realizations of intensity for $\sigma_\phi = 10.0$ and 31.6 radians for the power-law PSD and for $\sigma_\phi = 10.0$, 50.0, and 100 radians for the exponential PSD. The corresponding phase realizations are shown in Figures 25 and 26.

Figures 27 and 28 show the mean intensity PSD corresponding to intensities shown in Figures 23 and 24.

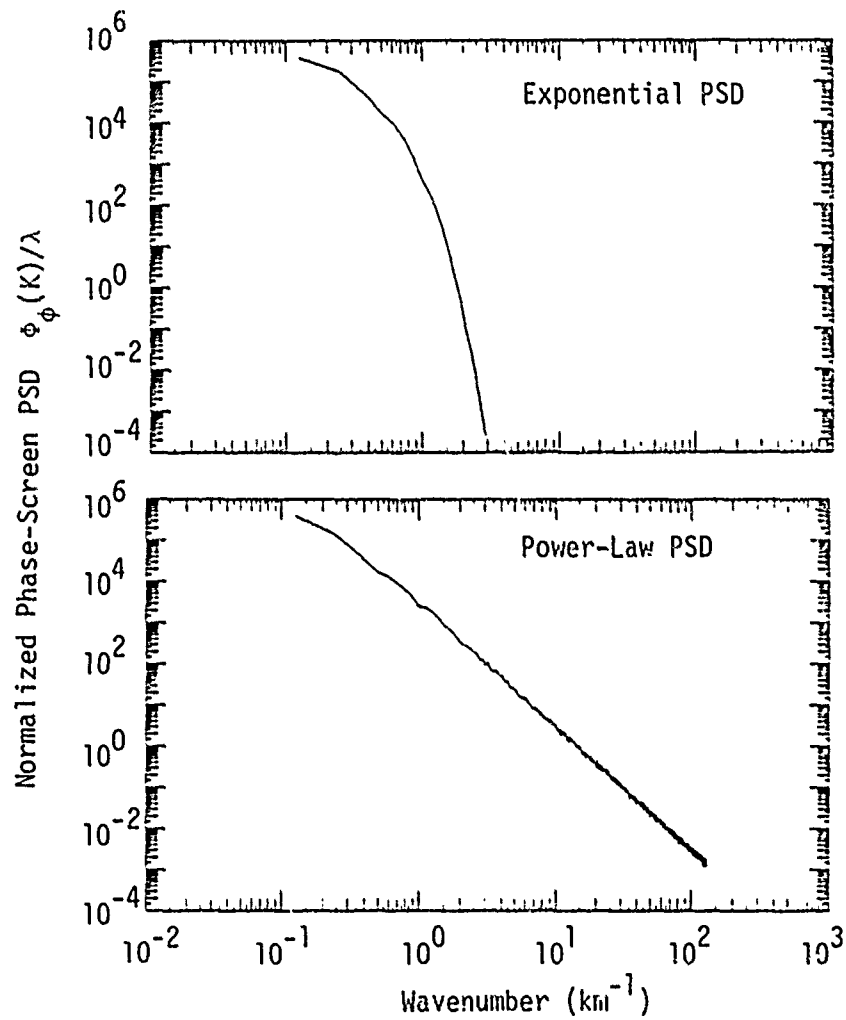


Figure 22. Comparison of simulation generated phase-screen PSD's for correlation length $\ell_c = 10$ km, $\lambda = 0.04$ m. ($\sigma_{\phi_i} = 10$ radians in figure).

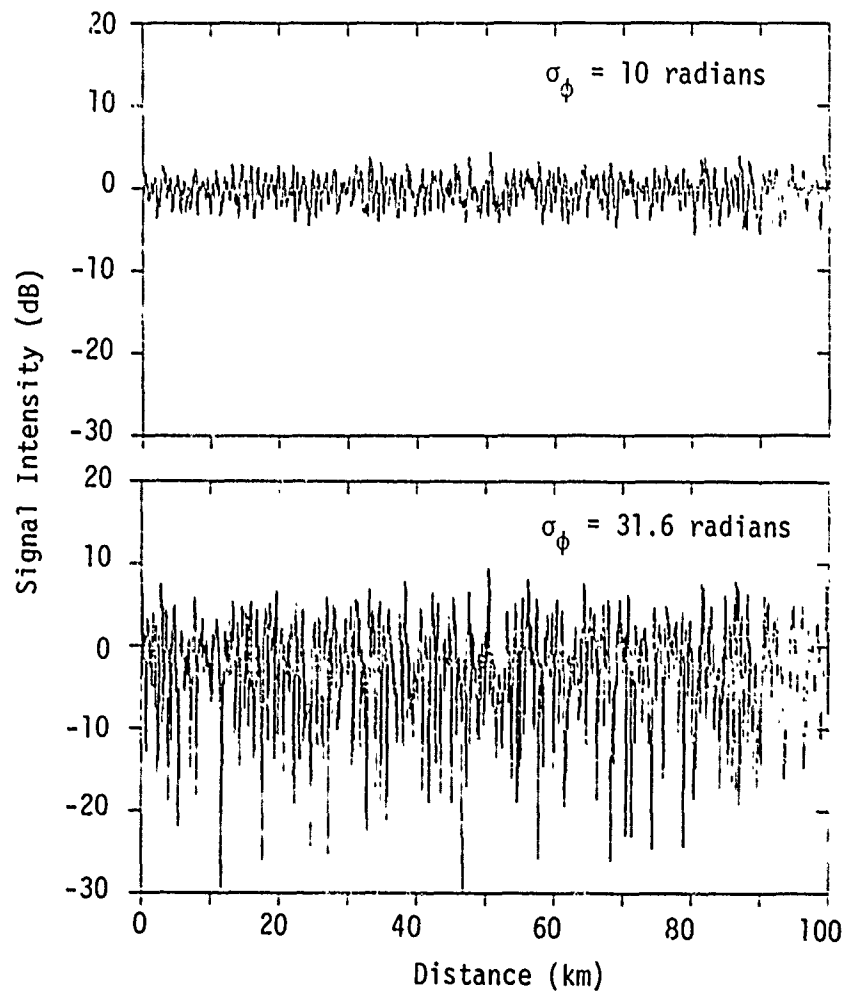


Figure 23. Realizations of signal intensity for power-law PSD with $\ell_c = 10$ km.

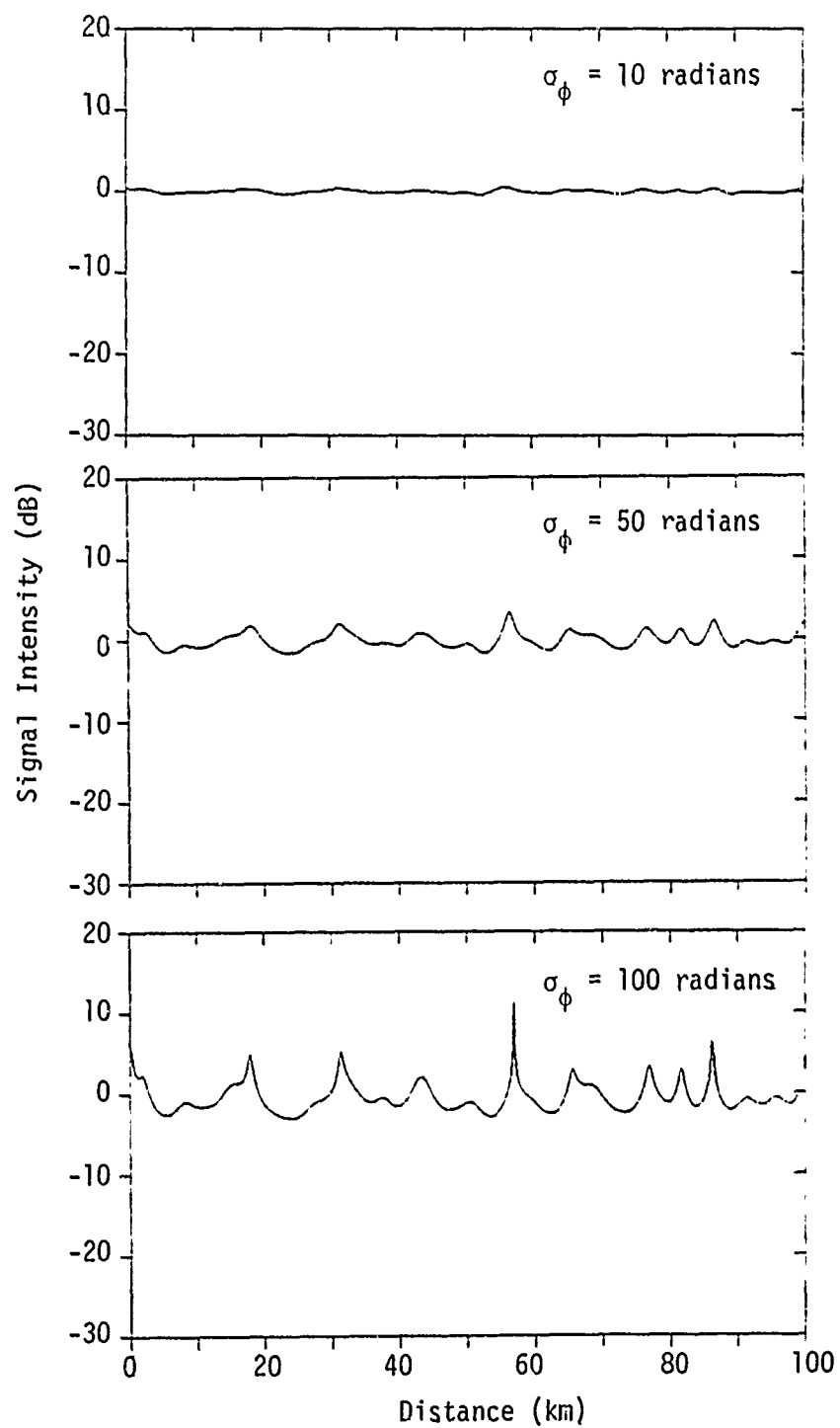


Figure 24. Realizations of signal intensity for exponential PSD with $\lambda_c = 10$ km.

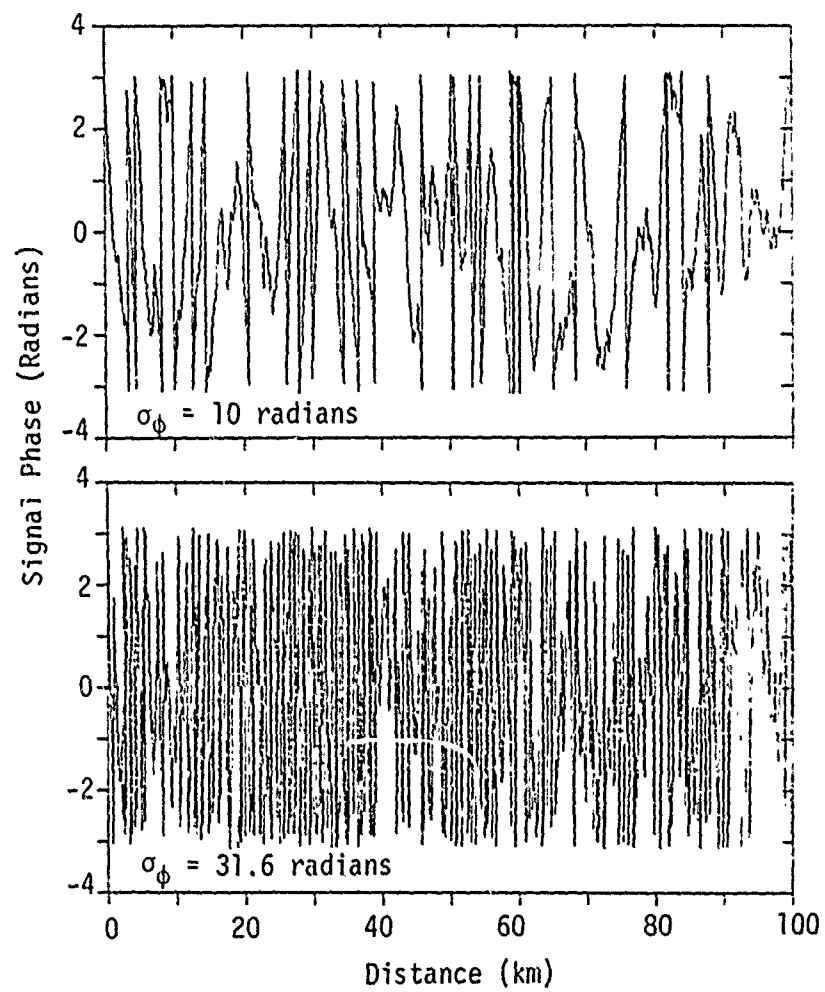


Figure 25. Realizations of signal phase for power-law PSD with $\ell_c = 10$ km.

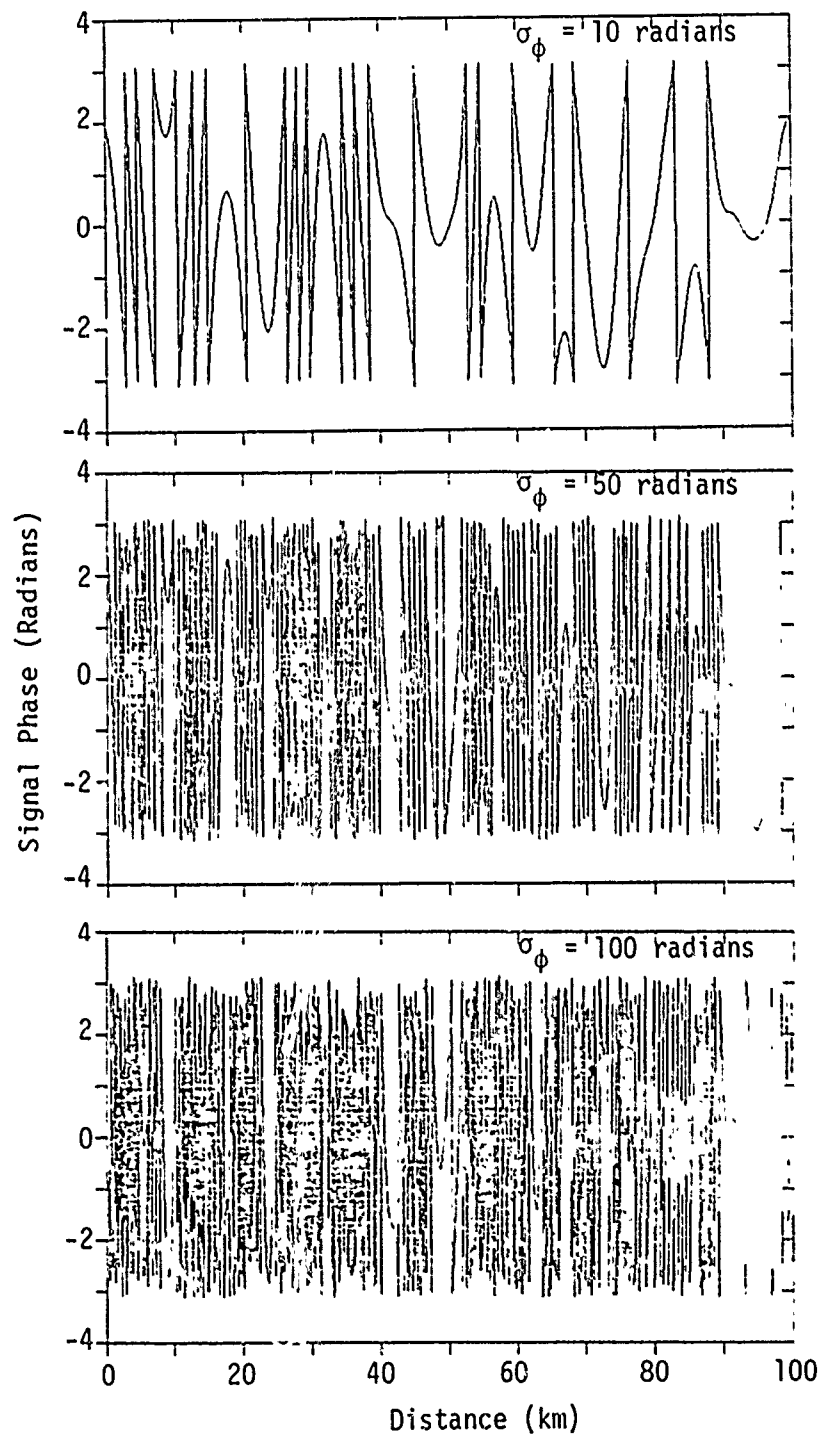


Figure 26. Realizations of signal phase for exponential PSD with $\lambda_c = 10$ km.

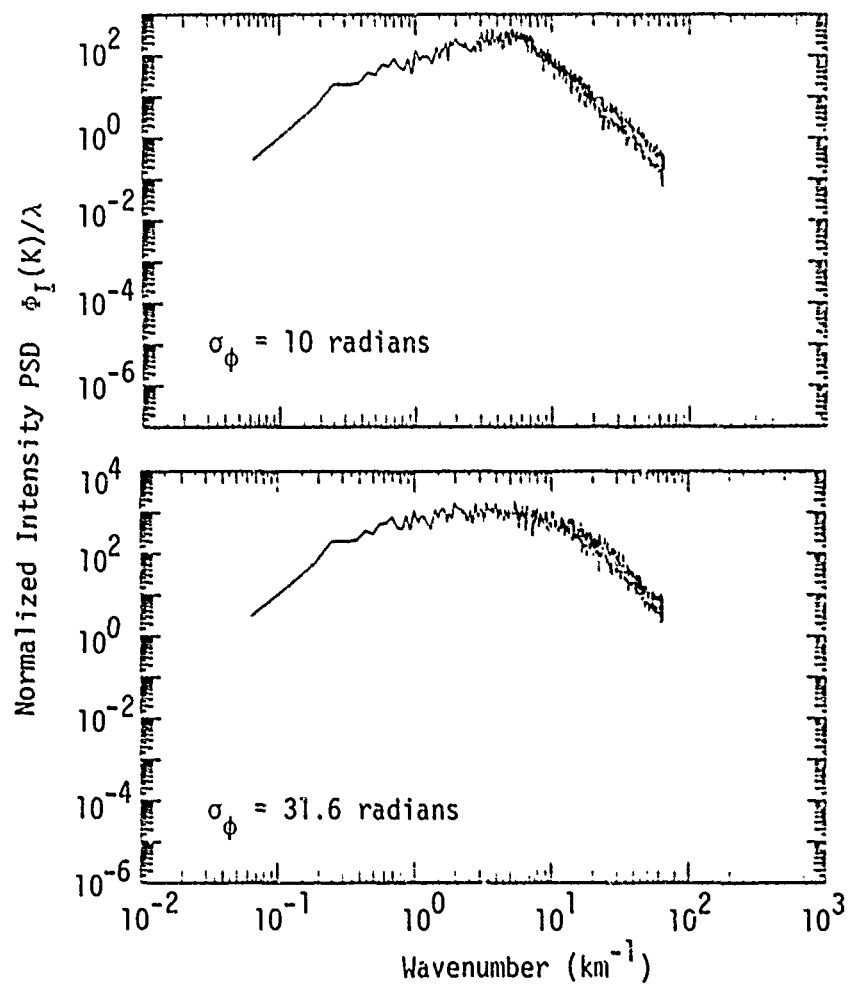


Figure 27. Normalized intensity PSD for power-law phase-screen PSD with $\ell_c = 10$ km, $\lambda = 0.04$ m.

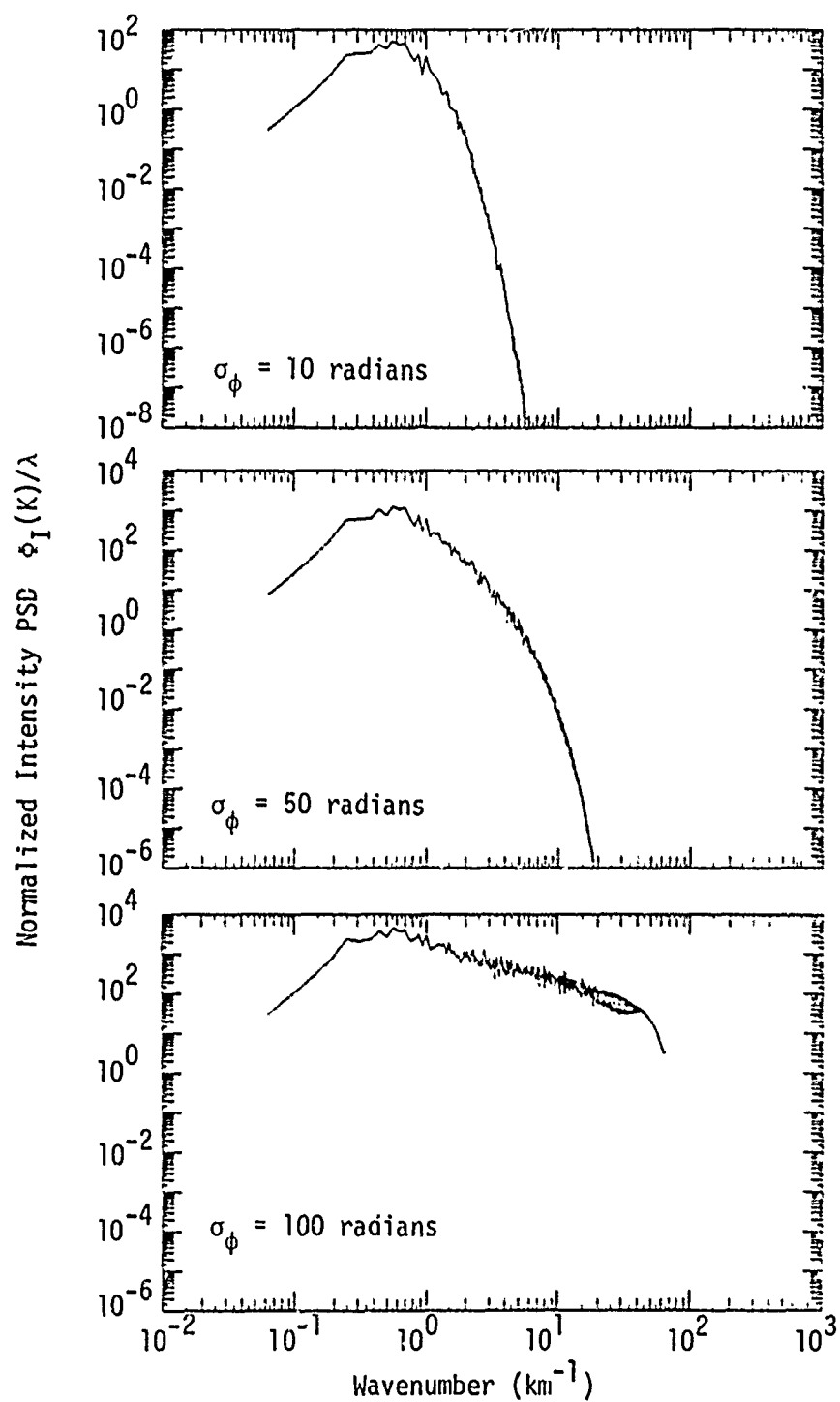


Figure 28. Normalized intensity PSD for exponential phase-screen PSD with $\ell_c = 10$ km, $\lambda = 0.04$ m.

SECTION 5

5.0 CONCLUSIONS

This report has presented and analyzed simulated results for electric field propagation through a thick, extended region of high-altitude striations of electron density. The simulated results correspond to the problem of communication from a DSCS satellite to a ground station at a frequency of 7.5 GHz. The results are parameterized in terms of the phase-screen power spectral density (PSD) and phase standard deviation σ_ϕ which may be related to the in-situ electron density PSD and electron density fluctuation σ_{N_e} by formulae developed in Appendix B. Statistical results are presented for S_4 scintillation index and intensity correlation length for a power-law and an exponential phase-screen PSD for values of phase standard deviation σ_ϕ ranging from 1 to 100 radians and phase correlation length ℓ_c ranging from 1 to 10 km.

Examples of specific realizations of the electric field amplitude and phase at the receiver are also shown. These realizations of signal structure are being used in simulations of DSCS receiver operation, reported elsewhere.

BIBLIOGRAPHY

1. Abramowitz, M. and I.A. Stegun (1970), Handbook of Mathematical Functions, Dover: New York.
2. Buckley, R. (1975), "Diffraction by a Random Phase-Changing Screen: A Numerical Experiment", J. of Atmospheric and Terrestrial Physics, Vol. 37, pp. 1431-1446.
3. Enslein, K., A. Ralston, and H.S. Wilf, (1977), Statistical Methods for Digital Computers, Wiley: New York.
4. Fante, R.L. (1975), "Electric Field Spectrum and Intensity Covariance of a Wave in a Random Medium", Radio Science, Vol. 10, No. 1, pp. 77-85.
5. Fante, R.L. (1977), "Effect of Source Bandwidth and Receiver Response Time on the Scintillation Index in Random Media", Radio Science, Vol. 12, No. 2, pp. 223-229.
6. Gradshteyn, I.S. and I.M. Ryzhik (1965), Tables of Integrals, Series, and Products, Academic Press: New York.
7. Hendrick, R.W. (1977) "Propagation Analysis for GPS", Mission Research Corporation, Report R-307.
8. Papoulis, A. (1965), Probability, Random Variables, and Stochastic Processes, McGraw-Hill: New York.
9. Ratcliffe, J.A. (1956), "Some Aspects of Diffraction Theory and Their Applications to the Ionosphere", in Reports on Progress in Physics, Volume 19, The Physical Society: London, England, pp. 188-267.
10. Rufenach, C.L. (1975), "Ionospheric Scintillation by a Random Phase Screen: Spectral Approach", Radio Science, Vol. 10, pp. 155-165.
11. Salpeter, E.E. (1967), "Interplanetary Scintillations. I. Theory", Ap. J., V. 147, pp. 433-448.
12. Whitney, H.E. and S. Basu (1977), "The Effect of Ionospheric Scintillation on VHF/UHF Satellite Communications", Radio Science, Vol. 12, No. 1, pp. 123-133.
13. Yeh, K.C., C.H. Liu and M.Y. Youakim, (1975), "A Theoretical Study of the Ionospheric Scintillation Behavior Caused by Multiple Scattering", Radio Science, Vol. 10, No. 1, pp. 97-106.

APPENDIX A

MULTIPLE PHASE SCREEN CODE

This Appendix describes the multiple phase screen propagation code as used to solve the scalar wave equation. Also included is a description of the technique used to generate the random phase-screens.

A.1 Scalar Wave Equation Solution

The problem of interest is that of a plane wave, incident at $z = 0$ on a random medium consisting of index of refraction fluctuations. Assume that the random medium extends from $z = 0$ to some distance and that its autocorrelation function is not a function of y . That is, the medium can be thought to consist of a number of random striations or tubes which are infinitely extended in the y -direction.

The propagating wave is then only a function of x and z . Ignoring depolarization, the scalar wave equation may be written

$$(\nabla^2 + k^2 n^2)\psi = 0 \quad (\text{A-1})$$

where

$$\nabla^2 = \frac{\partial^2}{\partial x^2} + \frac{\partial^2}{\partial z^2}$$

and $n = 1 + \Delta n$ is the index of refraction with Δn a small perturbation. The equation

$$\frac{\partial^2 u}{\partial z^2} + i2k \frac{\partial u}{\partial z} + \frac{\partial^2 u}{\partial x^2} + 2k^2 \Delta n u = 0 \quad (\text{A-2})$$

may be obtained from Equation A-1 using the substitution

$$\psi = u \exp(ikz) \quad (A-3)$$

and ignoring terms in $(\Delta n)^2$.

The complex amplitude u can vary markedly over distances no smaller than the inhomogeneity scale size ℓ ; that is, the worst case variation of u in the direction of propagation can be characterized by $u \sim \exp(-z^2/\ell_m^2)$ where $\ell_m \geq \ell$. Thus, the second derivative $\partial^2 u / \partial z^2$ is of the order of u/ℓ_m^2 . On the other hand, the second term of Equation A-2 is of the order of $u/\lambda \ell_m$. Therefore, for $\lambda \ll \ell_m$, or $\lambda \ll \ell$, the first term of Equation A-2 may be ignored with respect to the second term to obtain the parabolic wave equation

$$\frac{\partial^2 u}{\partial x^2} + i2k \frac{\partial u}{\partial z} + 2k^2 \Delta n u = 0 \quad (A-4)$$

Now for a given initial field, the propagation simulation must generate values of the field such that Equation A-4 is satisfied. To do this, the medium is divided into screens defined by planes on which z is constant. To propagate from one screen to the next write $u(x, z)$ in the form

$$u = w e^{\phi} \quad (A-5)$$

where

$$\phi(x, z) = ik \int_{z-\Delta z/2}^{z+\Delta z/2} dz' \Delta n(x, z') \quad (A-6)$$

so that

$$\frac{\partial \phi}{\partial z} = ik \Delta n(x, z) \quad (A-7)$$

Equations A-5 and A-7 may be substituted into Equation A-4 to obtain

$$e^{-\phi} \frac{\partial^2}{\partial x^2} (we^{\phi}) + 2ik \frac{\partial w}{\partial z} = 0 \quad (\text{A-8})$$

To solve this equation, assume that the step size Δz is sufficiently small so that the effect of the exponential factors in Equation A-8 is small. Thus, one can solve

$$\frac{\partial^2 w}{\partial x^2} + 2ik \frac{\partial w}{\partial z} = 0 \quad (\text{A-9})$$

A simple solution may be obtained using the Fourier transform relation

$$w(x, z) = \int_{-\infty}^{\infty} dK \hat{W}(K, z) e^{-ikx} \quad (\text{A-10})$$

which may be substituted into Equation A-9 to obtain

$$2ik \frac{\partial \hat{W}}{\partial z} - k^2 \hat{W} = 0 \quad (\text{A-11})$$

whose solution is

$$\hat{W}(K, z) = \hat{W}(K, 0) \exp \left(- \frac{iK^2}{2k} z \right) \quad (\text{A-12})$$

or using Equation A-12 in Equation A-10

$$w(x, z) = \int_{-\infty}^{\infty} dK \hat{W}(K, 0) \exp \left(- \frac{iK^2}{2k} z - ikx \right) \quad (\text{A-13})$$

Equation A-13 may be rewritten by applying Equation A-12 for $z = z_1$ and $z = z_2$ where z_1 and z_2 are two successive phase-screen locations

$$W(x, z_2) = \int_{-\infty}^{\infty} dK \hat{W}(K, z_1) \exp \left(- \frac{iK^2(z_2 - z_1)}{2k} - iKx \right) \quad (A-14)$$

Now, using Equation A-5 and Equation A-3 and replacing ψ by the electric field we obtain from Equation A-14

$$E(x, z_2) = e^{ik(z_2 - z_1)} \int_{-\infty}^{\infty} dK \hat{E}(K, z_1) \left(\exp - \frac{iK^2}{2k} (z_2 - z_1) - iKx \right) \quad (A-15)$$

where $E(K, z_1)$ is now the Fourier transform of the product

$$E(x, z_1) \exp \left\{ ik \int_{z_1 - \Delta z/2}^{z_1 + \Delta z/2} dz' \Delta n(x, z') \right\} \quad (A-16)$$

At this point it is interesting to note that one can obtain the Fresnel-Kirchhoff integral by substituting the Fourier transform

$$E(K, z_1) = \frac{1}{2\pi} \int_{-\infty}^{\infty} d\xi E(\xi, z_1) e^{iK\xi}$$

into Equation A-15 and performing the K integration (Gradshteyn and Ryzhik, p. 397) as

$$E(x, z_2) = \left(\frac{i2\pi(z_2 - z_1)}{k} \right)^{-1/2} \int_{-\infty}^{\infty} d\xi e^{ik(z_2 - z_1)} \times \exp \left\{ i \frac{1}{2} k(x - \xi)^2 / (z_2 - z_1) \right\} E(\xi, z_1) \quad (A-17)$$

The propagation simulation thus breaks up the random medium into a number of screens. The electric field incident on a phase-screen is then multiplied by the phase shift caused by the random medium lying between the

previous and current phase-screen (Equation A-12). The wave then propagates as if in free space to the next phase-screen (Equation A-11). Propagation from one phase-screen to the next is accomplished very efficiently by the use of the fast Fourier transform so that once the electric field is multiplied by the appropriate complex phase term (as in Equation A-12) its Fourier transform is taken, multiplied by $\exp(-ik^2(z_2-z_1)/k)$ and then another fast Fourier transform is performed to obtain the electric field at the next screen $E(x, z_2)$.

A.2 Generation of the Random Phase Screen

The following procedure taken from Buckley (1975) was used to generate the random phase screen with arbitrary variance and power spectral density.

Assume that P_i is a sequence of random numbers uniformly distributed between $-1/2$ and $1/2$. Then

$$\begin{aligned}\langle P_i \rangle &= 0 \\ \langle P_i P_j \rangle &= \frac{1}{12} \delta_{ij}\end{aligned}\tag{A-18}$$

where δ_{ij} is the Kronecker delta function. Now choose the phase as a sequence given by the circular (see Enslein, et al., p. 380) correlation

$$\phi_\ell = \phi(\ell \Delta x) = \sum_{j=0}^{N-1} w_j P_{j+\ell}; \ell = 0, N-1\tag{A-19}$$

where the phase screen is sampled at increments $\Delta x = L/N$ where L is the total length of the screen. The w_j are a set of weights which are to be determined.

Since each value ϕ_ℓ is a sum of a large number N of independent random variables, it follows from the central limit theorem that the sequence $\{\phi_\ell\}$ will possess a Gaussian distribution with zero mean. Now the phase autocorrelation function ρ_K may be formed by noting

$$\begin{aligned}\langle \phi_i \phi_{i+k} \rangle &= \left\langle \sum_{j=0}^{N-1} w_j P_{j+i} \sum_{\ell=0}^{N-1} w_\ell P_{\ell+i+k} \right\rangle \\ &= \sum_{j=0}^{N-1} w_j \sum_{\ell=0}^{N-1} w_\ell \frac{1}{12} \delta_{j, \ell+k} \\ &= \frac{1}{12} \sum_{\ell=0}^{N-1} w_\ell w_{\ell+k}\end{aligned}\tag{A-20}$$

Set

$$\phi_0^2 \equiv \langle \phi_i \phi_i \rangle = \frac{1}{12} \sum_{\ell=0}^{N-1} w_\ell^2\tag{A-21}$$

to obtain the autocorrelation function

$$\begin{aligned}\rho_K &\equiv \frac{1}{\phi_0^2} \langle \phi_i \phi_{i+k} \rangle \\ \rho_K &= \frac{1}{12\phi_0^2} \sum_{\ell=0}^{N-1} w_\ell w_{\ell+k} \quad k=0, \dots, N-1\end{aligned}\tag{A-22}$$

The ρ_K sequence may be interpreted as

$$\rho(k\Delta x), \quad k = 0, \dots, N-1; \text{ that is, } \rho_K$$

is a discrete representation of the continuous autocorrelation function.

Now in order to relate the still unknown weights $\{w_k, k=0, \dots, N-1\}$ to the power spectral density of the phase we must use the Fourier transform pair

$$\rho(x) = \int_{-\infty}^{\infty} S(K) e^{-iKx} dK \quad (A-23)$$

$$S(K) = \frac{1}{2\pi} \int_{-\infty}^{\infty} \rho(x) e^{iKx} dx \quad (A-24)$$

and their discrete representations

$$\rho(k\Delta x) = 2\pi\Delta Q \sum_{\ell=0}^{N-1} S(\ell 2\pi\Delta Q) e^{-i(k\Delta x)(\ell 2\pi\Delta Q)}, \quad k=0, \dots, N-1 \quad (A-25)$$

$$S(\ell 2\pi\Delta Q) = \frac{\Delta x}{2\pi} \sum_{k=0}^{N-1} \rho(k\Delta x) e^{+i(k\Delta x)(\ell 2\pi\Delta Q)}, \quad \ell=0, \dots, N-1 \quad (A-26)$$

where $\Delta K = 2\pi\Delta Q$. Noting that $\Delta x = L/N$, where L is the length of a phase screen, $\Delta Q = 1/L$, $\Delta x\Delta Q = 1/N$, Equation A-25 and Equation A-26 may be rewritten as

$$\rho_k = \rho(k\Delta x) = 2\pi\Delta Q \sum_{\ell=0}^{N-1} S_{\ell} e^{-i2\pi k\ell/N}, \quad k=0, \dots, N-1 \quad (A-27)$$

$$S_{\ell} = \delta(\ell 2\pi\Delta Q) = \frac{\Delta x}{2\pi} \sum_{k=0}^{N-1} \rho_k e^{+i2\pi k\ell/N}, \quad \ell=0, \dots, N-1 \quad (A-28)$$

Now the Fourier transfer of Equation A-22 is given by

$$S_r = \frac{\Delta x}{2\pi} \frac{1}{12\phi_0^2} \sum_{k=0}^{N-1} \sum_{\ell=0}^{N-1} w_{\ell+k} e^{i2\pi k r/N} \quad (A-29)$$

The Fourier transform of the weight is given by \hat{w} as

$$w_\ell = 2\pi\Delta Q \sum_{m=0}^{N-1} \hat{w}_m e^{-i2\pi m\ell/N} \quad (\text{A-30})$$

and similarly for $w_{\ell+k}$

$$w_{\ell+k} = 2\pi\Delta Q \sum_{n=0}^{N-1} \hat{w}_n e^{-i2\pi(\ell+k)n/N} \quad (\text{A-31})$$

Now since the weights $\{w_k\}$ are real $w_\ell = w_\ell^*$ and we can use the complex conjugate of Equation A-30 and Equation A-31 with Equation A-29 to obtain

$$S_r = \frac{4\pi^2 (\Delta Q)^2 \Delta x}{24\pi\phi_0^2} \sum_k \sum_\ell \sum_m \sum_n \hat{w}_m^* e^{+i2\pi m\ell/N} \hat{w}_n e^{-i2\pi(\ell+k)n/N} e^{i2\pi kr/N} \quad (\text{A-32})$$

Now since

$$\sum_{\ell=0}^{N-1} e^{-i2\pi\ell n/N} e^{i2\pi m\ell/N} = N\delta_{mn}$$

$$\sum_{k=0}^{N-1} e^{-i2\pi kn/N} e^{i2\pi kr/N} = N\delta_{nr} \quad (\text{A-33})$$

Equation A-32 may be summed to yield

$$S_r = \frac{\pi(\Delta Q)^2 \Delta x N^2}{6\phi_0^2} |\hat{w}_r|^2 \quad (\text{A-34})$$

or since $N\Delta Q = 1/\Delta x$ the Fourier transform of the weights is given by:

$$\hat{w}_r = \sqrt{\frac{6\Delta x\phi_0^2}{\pi}} S_r \quad (\text{A-35})$$

where S_r is the discrete Fourier transform representation of the phase-screen power spectral density.

Thus, to generate the phase values for a phase-screen, one may start with the power spectral density, obtain the Fourier transform of the weights via Equation A-35, and take the inverse Fourier transform to obtain the weights themselves.

APPENDIX B

RELATIONSHIP BETWEEN PHASE AND ELECTRON NUMBER DENSITY

B.1 Phase Screen PSD Related to Electron Density PSD

As discussed in Appendix A, the electric field at each phase screen is multiplied by the factor $e^{i\phi(x)}$ where

$$\phi(x) = k \int_{-\frac{\Delta z}{2}}^{\frac{\Delta z}{2}} \Delta n(x, z) dz \quad (B-1)$$

which effectively collapses the index-of-refraction fluctuations in the region from $-\Delta z/2$ to $\Delta z/2$. In the absence of significant electron collisions, the index of refraction is given as

$$n^2 = 1 - \frac{N_e}{n^*} \quad (B-2)$$

where N_e is the electron number density and n^* is the critical electron number density

$$n^* = \frac{\epsilon_0 m_e \omega^2}{e^2} = 1.24 \times 10^{-8} f^2 \text{ [el/cm}^3\text{]} \quad (B-3)$$

where ϵ_0 is the permittivity of free space, m_e is the mass of an electron, e is the electron charge, and f is the radio frequency in Hertz. From Equation B-2, the deviation in refractive index is, for $N_e \ll n^*$

$$\Delta n = \frac{1}{2} \frac{\Delta N_e}{n^*} \quad (B-4)$$

so that Equation B-1 can be written as

$$\phi(x) = \frac{1}{2} \frac{k}{n^*} \int_{-\frac{\Delta z}{2}}^{\frac{\Delta z}{2}} \Delta N_e(x, z) dz \quad (B-5)$$

Now the autocorrelation function can be formed as

$$\begin{aligned} \sigma_\phi^2 B_\phi(\xi) &= \langle \Delta\phi(x) \Delta\phi(x+\xi) \rangle \\ &= \frac{1}{4} \frac{k^2}{n^{*2}} \int_{-\frac{\Delta z}{2}}^{\frac{\Delta z}{2}} \int_{-\frac{\Delta z}{2}}^{\frac{\Delta z}{2}} \langle \Delta N_e(x, z) \Delta N_e(x+\xi, z') \rangle dz dz' \\ &= \frac{\sigma_{N_e}^2 k^2}{4 n^{*2}} \int_{-\frac{\Delta z}{2}}^{\frac{\Delta z}{2}} \int_{-\frac{\Delta z}{2}}^{\frac{\Delta z}{2}} B_{N_e}(\xi, z-z') dz dz' \end{aligned} \quad (B-6)$$

The double integral here can be reduced to a single integration by a change of variables as explained by Parulis (1965), page 325 as

$$\sigma_\phi^2 B_\phi(\xi) = \frac{\sigma_{N_e}^2 k^2}{4 n^{*2}} \Delta z \int_{-\Delta z}^{\Delta z} \left(1 - \frac{|n|}{\Delta z}\right) B_{N_e}(\xi, \eta) d\eta \quad (B-7)$$

If Δz is greater than the correlation length of the electron density fluctuations, then the contribution of the second term in the integration will always be negligible so that

$$\sigma_{\phi}^2 B_{\phi}(\xi) = \frac{\sigma_{N_e}^2 k^2}{4 n^{*2}} \Delta z \int_{-\infty}^{\infty} B_{N_e}(\xi, \eta) d\eta \quad (B-8)$$

Now, by multiplying both sides of Equation B-8 by $e^{iK_x \xi} / 2\pi$ and integrating with respect to ξ and using the Fourier transform relationship given by Equations B-11 and B-14 and their 2-D extensions one obtains

$$\Phi_{\phi}(K_x) = 2\pi \Delta z \frac{1}{4} \frac{k^2}{n^{*2}} \Phi_{N_e}(K_x, K_z = 0) \quad (B-9)$$

Equation B-9 is a general relationship between the phase spectrum and the 2-dimensional electron density spectrum.

Setting $F = 0$ in Equation B-8 and noting that $B_{\phi}(0) = 1$ gives the relationship between the variance of phase and the variance of electron density fluctuations

$$\sigma_{\phi}^2 = \frac{\sigma_{N_e}^2 k^2}{4 n^{*2}} \Delta z \int_{-\infty}^{\infty} B_{N_e}(0, \eta) d\eta \quad (B-10)$$

B.2 One, Two and Three Dimensional Power Spectra

Given an isotropic and homogeneous random medium with the autocorrelation functions $B_1(x)$, $B_2(\rho)$, and $B_3(r)$ in one, two, and three-dimensions, then the respective power spectral densities are:

$$\Phi_1(K) = \frac{\sigma^2}{2\pi} \int_{-\infty}^{\infty} dx \cos Kx B_1(x) \quad (B-11)$$

$$\Phi_2(K) = \frac{\sigma^2}{2\pi} \int_0^{\infty} \rho d\rho J_0(K\rho) B_2(\rho) \quad (B-12)$$

$$\phi_3(K) = \frac{\sigma^2}{2\pi^2 K} \int_0^\infty dr \, r \sin Kr \, B_3(r) \quad (B-13)$$

which have the inverse transforms:

$$\sigma^2 B_1(x) = \int_{-\infty}^\infty dK \cos Kx \, \phi_1(K) \quad (B-14)$$

$$\sigma^2 B_2(\rho) = 2\pi \int_0^\infty dK \, K J_0(K\rho) \, \phi_2(K) \quad (B-15)$$

$$\sigma^2 B_3(r) = \frac{4\pi}{r} \int_0^\infty dK \, K \sin Kr \, \phi_3(K) \quad (B-16)$$

where the subscripts again denote the dimensionality.

These relationships above are consistent with the relationships between the spectra in various dimensions (Rufenach, 1975):

$$\phi_2(K_x, K_y) = \int dK_z \, \phi_3(K_x, K_y, K_z) \quad (B-17)$$

$$\phi_1(K_x) = \int dK_y \, \phi_2(K_x, K_y) \quad (B-18)$$

Under the assumption that the autocorrelation function has the same form in one, two, or three dimensions, the following relationships are easily shown for some common autocorrelation functions. Only the 3-dimensional form of the autocorrelation function is specified.

1. Exponential Autocorrelation Function

$$B(r) = \exp \left\{ -|r|/r_0 \right\} \quad (B-19)$$

$$\phi_1(k) = \frac{\sigma_{Ne}^2}{\pi} \frac{r_0}{1+k^2 r_0^2} \quad (B-20)$$

$$\phi_2(k) = \frac{\sigma_{Ne}^2}{2\pi} \frac{r_0^2}{(1+k^2 r_0^2)^{3/2}} \quad (B-21)$$

$$\phi_3(k) = \frac{\sigma_{Ne}^2}{\pi^2} \frac{r_0^3}{(1+k^2 r_0^2)^2} \quad (B-22)$$

2. Power-Law Autocorrelation Functions

$$B(r) = \frac{1}{\left(1 + \frac{r^2}{r_0^2} \right)^{\frac{n-3}{2}}} \quad (B-23)$$

(n need not be an integer)

$$\phi_1(K) = \sigma_{N_e}^2 \frac{2^{\frac{4-n}{2}} r_0^{\frac{n-4}{2}}}{\pi^{1/2} \Gamma(\frac{n-3}{2})} (Kr_0)^{\frac{n-4}{2}} K_{\frac{n-4}{2}}(Kr_0), \quad (B-24)$$

$$\phi_2(K) = \sigma_{N_e}^2 \frac{2^{\frac{3-n}{2}} r_0^{\frac{n-5}{2}}}{\pi \Gamma(\frac{n-3}{2})} (Kr_0)^{\frac{n-5}{2}} K_{\frac{n-5}{2}}(Kr_0), \quad (B-25)$$

$$\phi_3(K) = \sigma_{N_e}^2 \frac{2^{\frac{2-n}{2}} r_0^{\frac{n-6}{2}}}{\pi^{3/2} \Gamma(\frac{n-3}{2})} (Kr_0)^{\frac{n-6}{2}} K_{\frac{n-6}{2}}(Kr_0), \quad (B-26)$$

where $K(x)$ is the Bessel function of the third kind.

B.3 Two Dimensional K^{-2} in-situ N_e Spectrum

$\phi_{\phi}^{(1)}(K)$, the one-dimensional power law phase power spectral density used in this report may be derived by assuming an in-situ K^{-2} spectrum for electron density fluctuations as given by Equation B-20. Then, Equation B-21 and Equation B-9 yield the phase power spectral density

$$\phi_{\phi}(K) = \frac{2\pi\Delta z}{4n^*2} \frac{k^2}{2\pi} \frac{\sigma_{N_e}^2}{(1+K^2 r_0^2)^{3/2}} \quad (B-27)$$

The integral specified by Equation B-10 may be performed using Equation B-19 as the autocorrelation function to obtain

$$\sigma_{\phi}^2 = \frac{r_0^2 k^2 \Delta z}{2n^*2} \sigma_{N_e}^2 \quad (B-28)$$

or using Equation B-28 in Equation B-27 one comes full circle to obtain

$$\phi_{\phi}(K) = \sigma_{\phi}^2 \frac{r_0}{2} \frac{1}{(1+K^2 r_0^2)^{3/2}} \quad (B-29)$$

which is identical to Equation 1-1 with r_0 replaced by L_0 .

B.4 Two-dimensional Exponential in-situ N_e Spectrum

$\phi_{\phi}^{(2)}(K)$, the one-dimensional exponential phase PSD given by Equation 1-2 may be obtained from Equation B-25 with $n = 6$ so that Equation B-25 represents a two-dimensional exponential PSD for electron density fluctuations

$$\phi_{N_e}(K) = \sigma_{N_e}^2 \frac{r_0^2}{2\pi} e^{-Kr_0} \quad (B-30)$$

The autocorrelation function is then

$$B_{N_e}(r) = \frac{1}{(1+(r/r_0)^2)^{3/2}} \quad (B-31)$$

So that the phase PSD may be determined as

$$\phi_{\phi}(K) = \sigma_{\phi}^2 \frac{r_0}{2} e^{-Kr_0} \quad (B-32)$$

where

$$\sigma_{\phi}^2 = \frac{r_0 k^2 \Delta z}{2n^2} \sigma_{N_e}^2 \quad (B-33)$$

APPENDIX C

PHASE-SCREEN REALIZATIONS

For all the 7.5 GHz DSCS simulation results presented in this report the striated region was modeled by ten phase-screens and the simulation was run ten times, each time with a different set of phase-screen realizations, to obtain statistical results. This Appendix shows all ten phase-screens used for the first realization and also the observed intensity at each screen so that the reader may "watch" as the wave propagates through the medium to the receiver plane. For this case the exponential PSD given by Equation 1-2 with a phase standard deviation $\sigma_\phi = 31.6$ radians and a correlation length $\ell_c = 3.0$ km is used.

The 10 phase screens are shown in Figure C-1 (a-d) as a function of distance z from the top of the disturbed region (see Figure 1 (a)).

Figure C-2 (a-d) shows the intensity observed at the second through tenth phase screen location (the intensity at the first phase-screen location is a constant) and at the receiver plane located 300 km from the tenth phase screen. It is interesting to try to trace the focusing effects which are occurring as the wave propagates through the screen. The Gaussian irregularity denoted by an arrow on the first phase screen ($z = 0$, Figure C-1(a)) can be seen to be the cause of the intensity diffraction pattern which is traceable for $z = 3,300$ km to $z = 15000$ km and denoted by arrows on each observation screen.

This realization of all ten screens can be used as another visual test of the accuracy of the simulation by using the Fresnel-Kirchhoff equation to analytically compute the diffraction pattern of the Gaussian lens shown in Figure C-3. The diffraction pattern is shown as a function of z on the same scale as used in Figure C-2 and shows a striking resemblance to the results generated for the random screen realization.

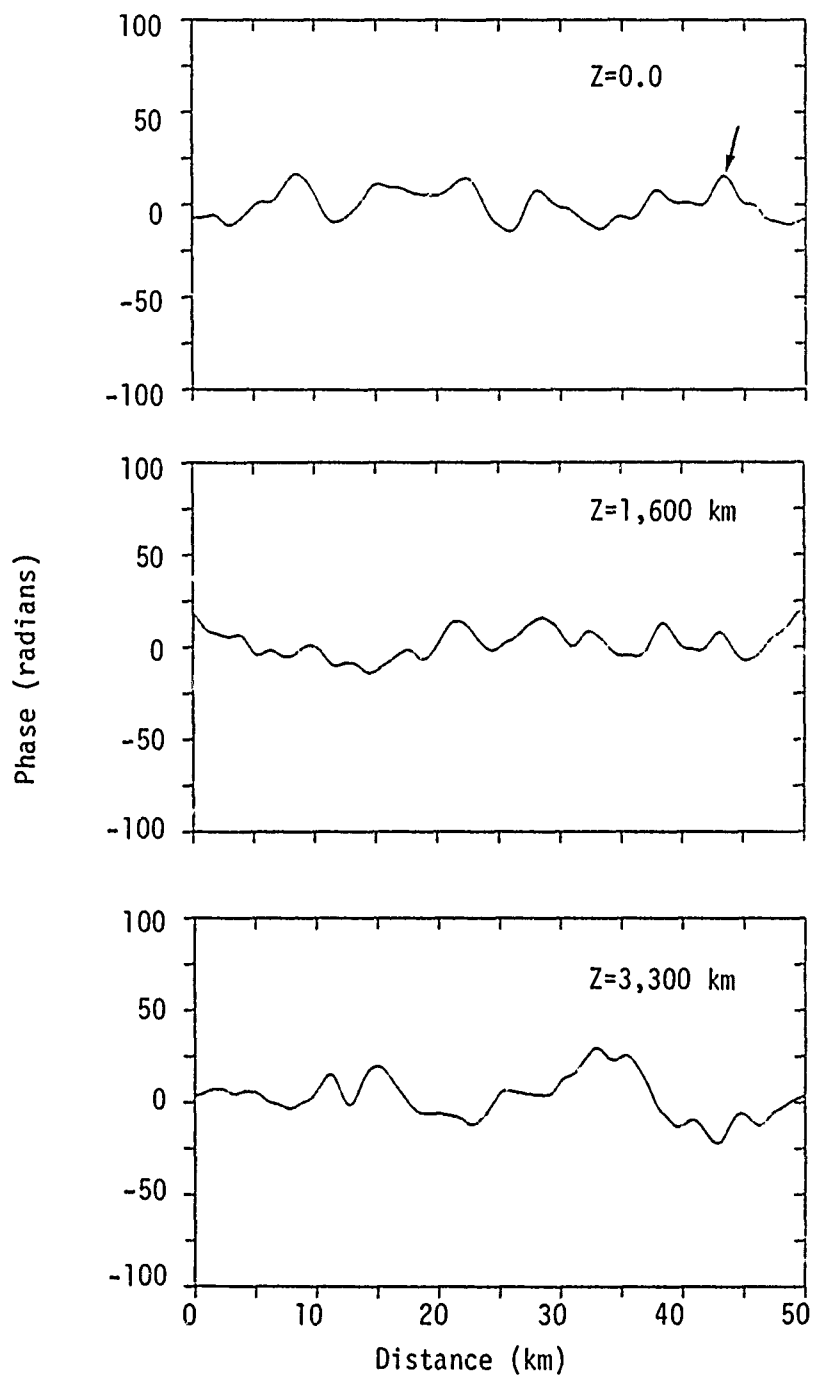


Figure C-1(a). Realizations of phase-screens with exponential PSD ($\sigma_\phi = 31.6 \text{ rad}$, $\ell_c = 3 \text{ km}$).

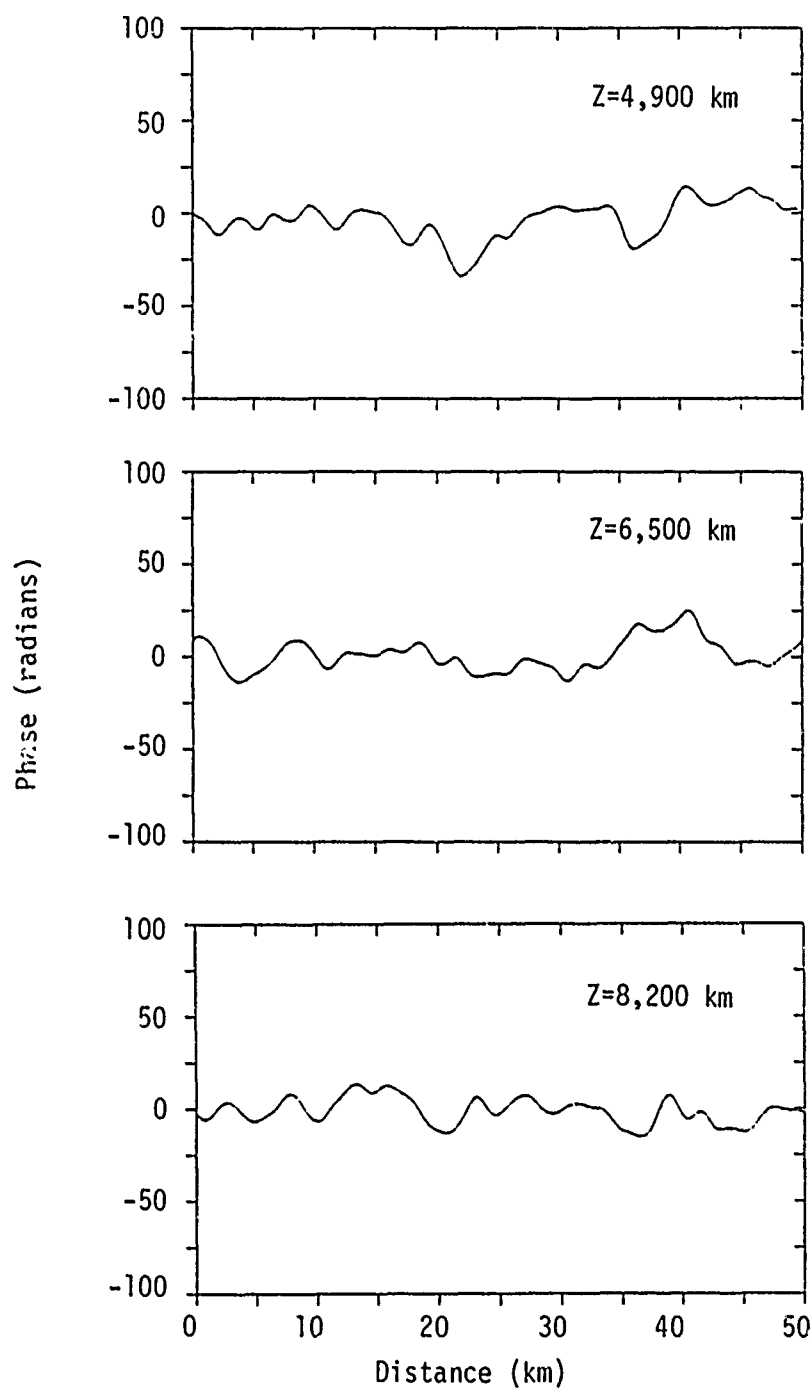


Figure C-1(b). Realizations of phase-screens with exponential PSD ($\sigma_\phi = 31.6$ rad, $\ell_c = 3$ km).

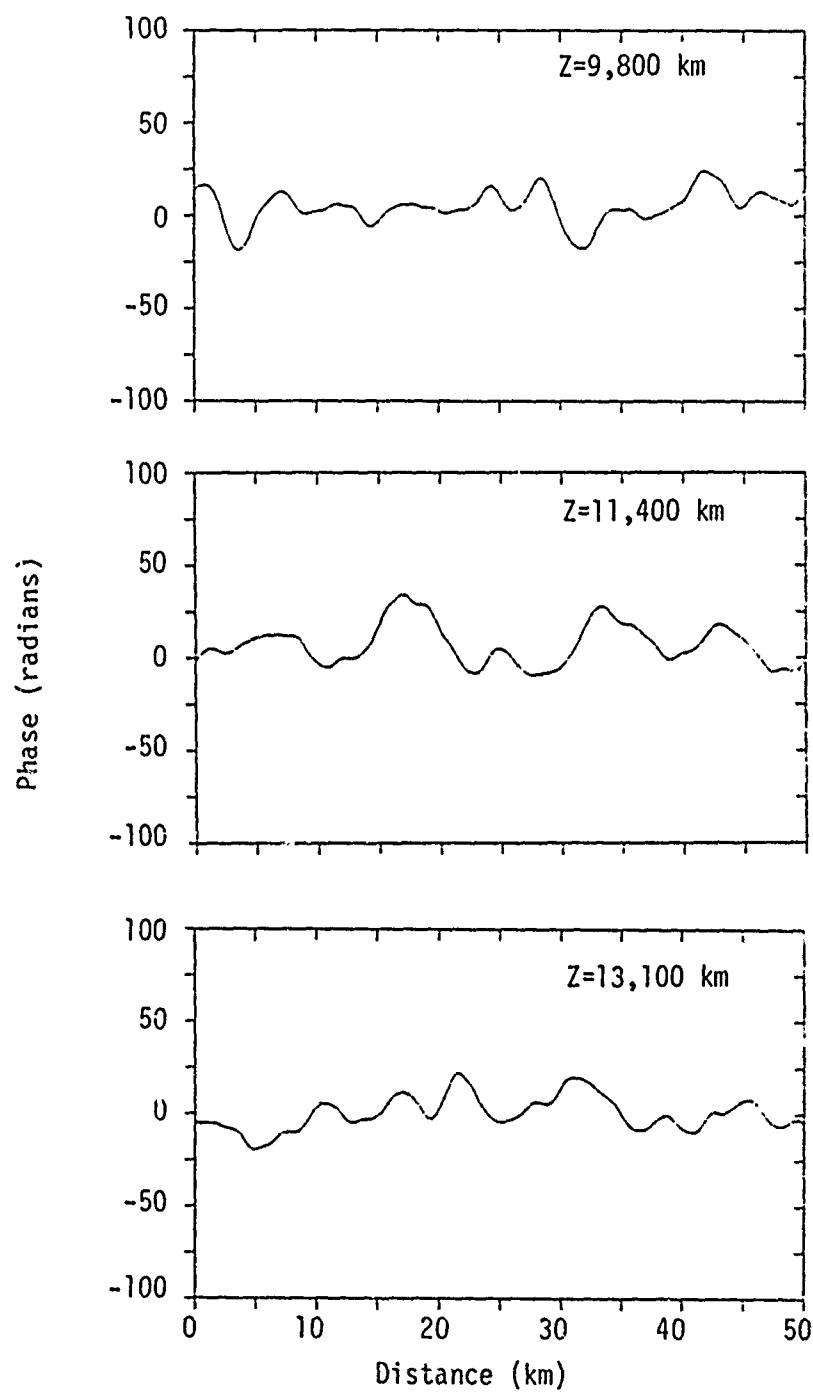


Figure C-1(c). Realizations of phase-screens with exponential PSD ($\sigma_\phi = 31.6$ rad, $\ell_c = 3$ km).

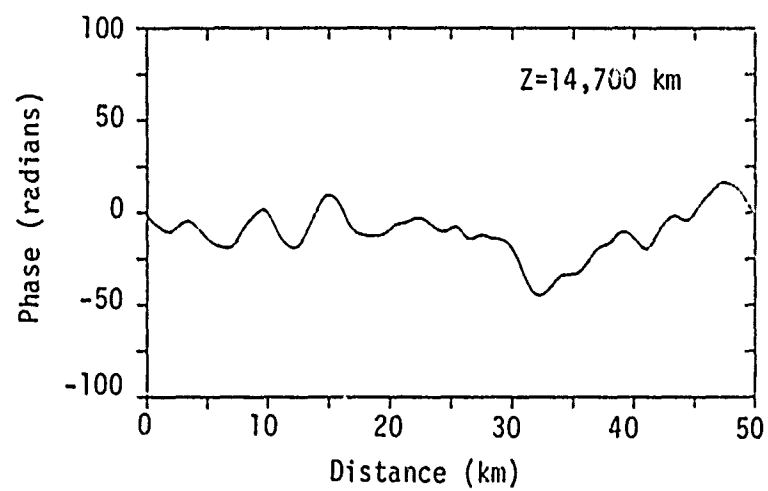


Figure C-1(d). Realizations of phase-screens with exponential PSD ($\sigma_{\phi} = 31.6$ rad, $\ell_c = 3$ km).

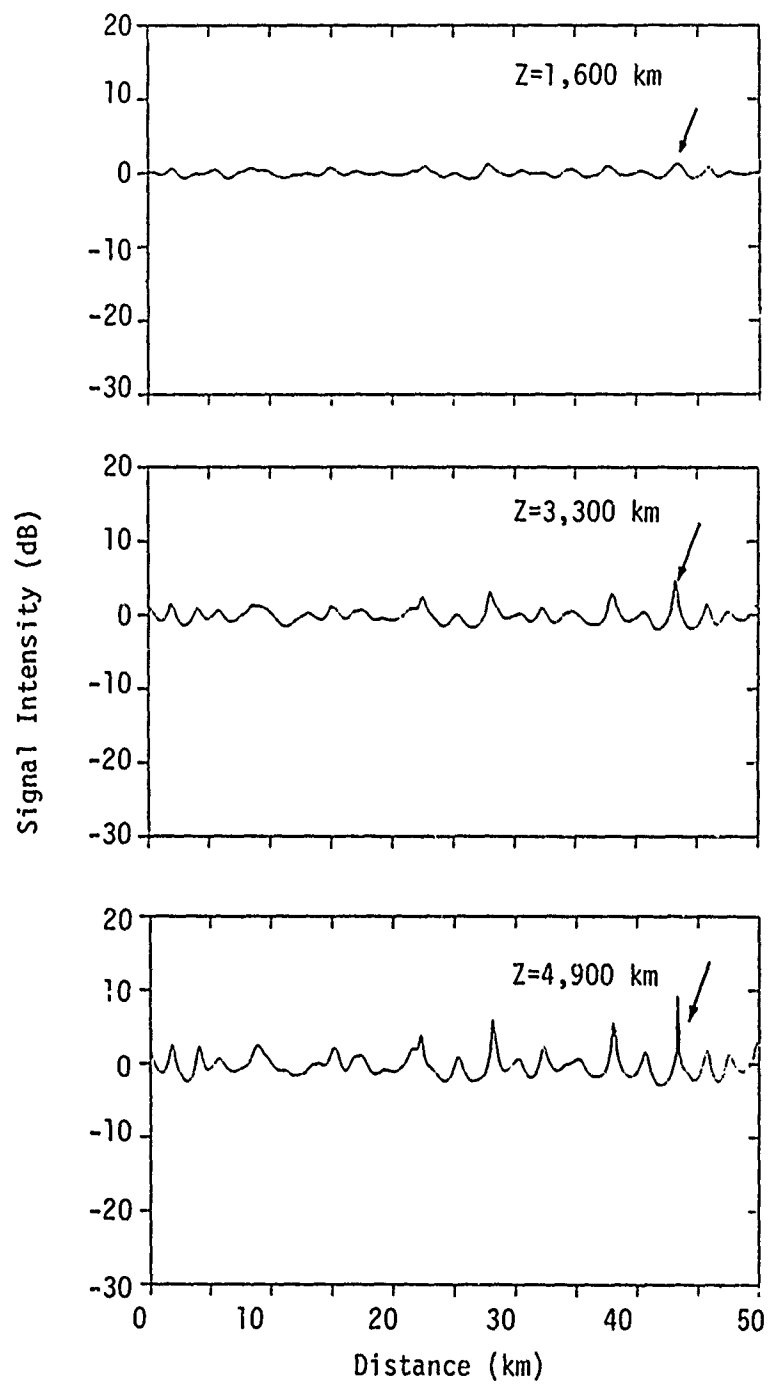


Figure C-2 (a). Realizations of intensity at each observation screen location.

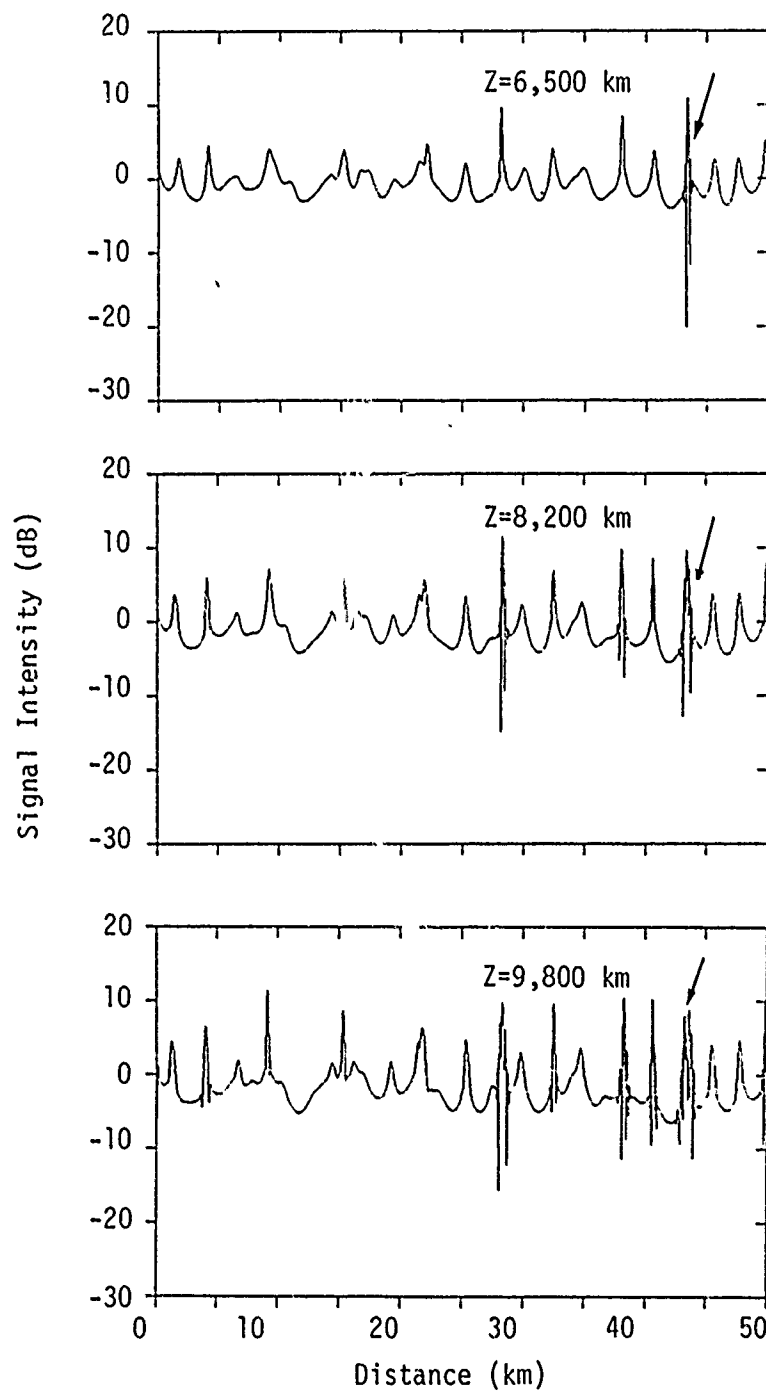


Figure C-2 (b). Realizations of intensity at each observation screen location.

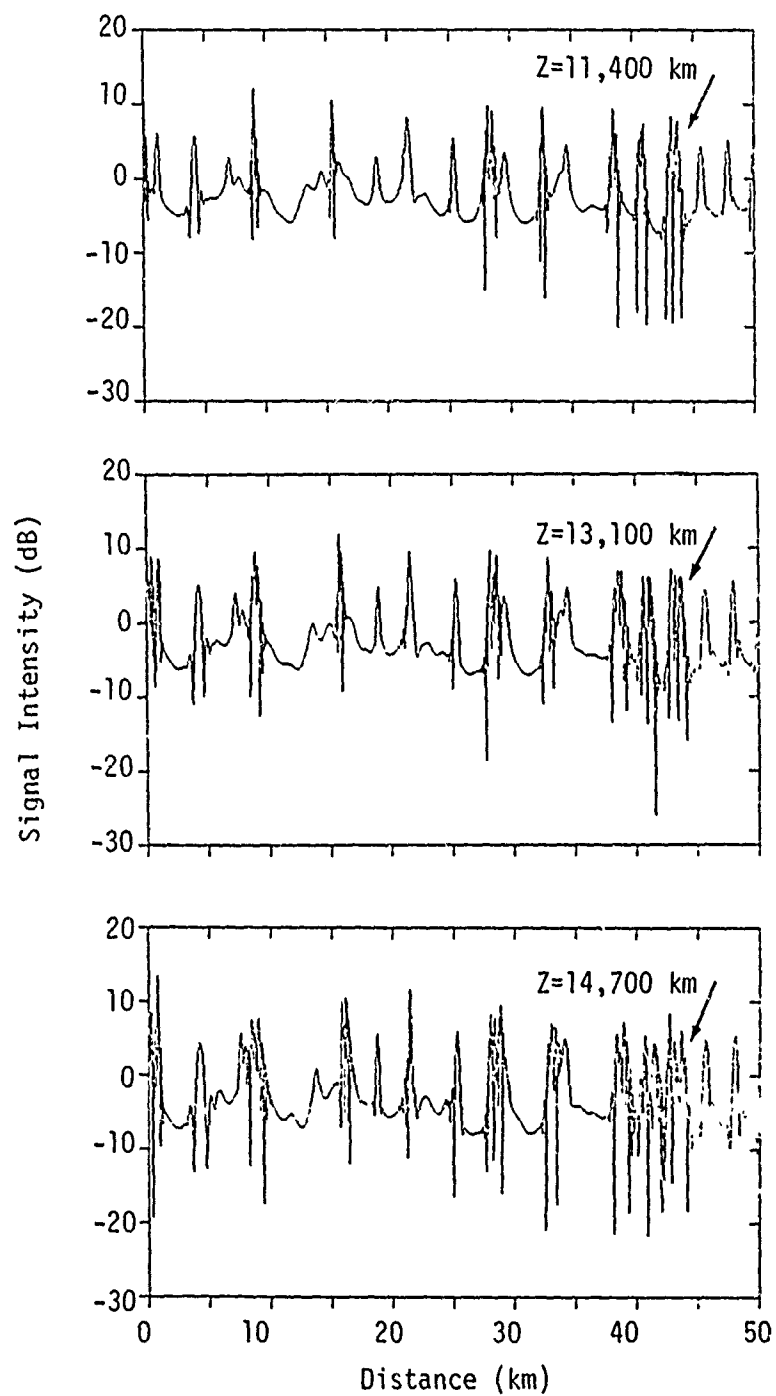


Figure C-2 (c). Realizations of intensity at each observation screen location.

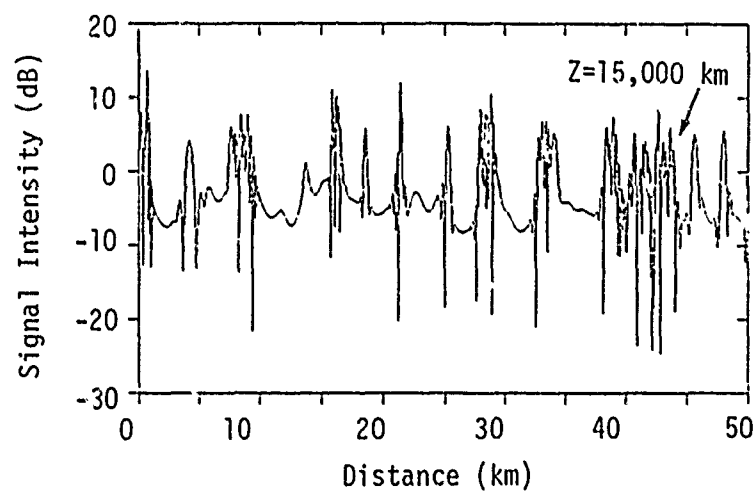


Figure C-2 (d). Realizations of intensity at each observation screen location.

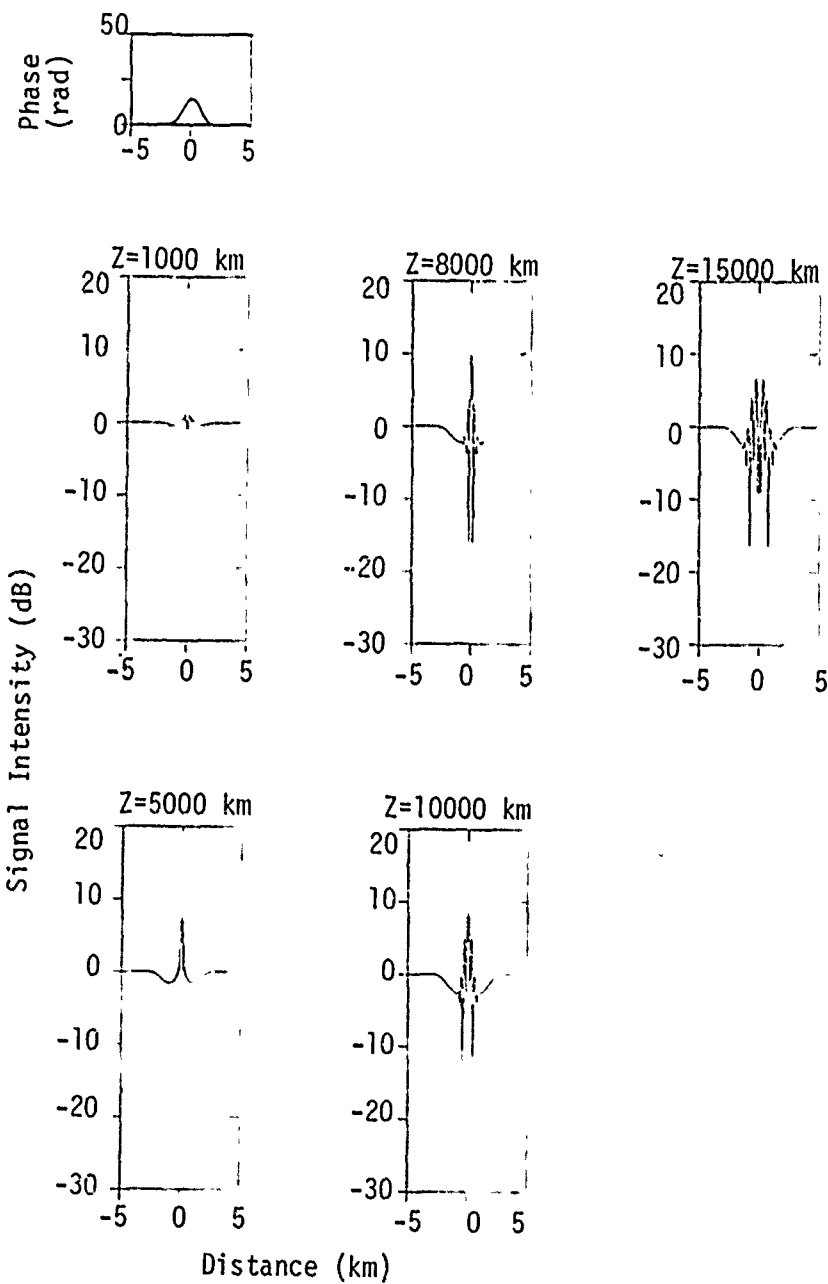


Figure C-3. Analytic diffraction pattern of a Gaussian lens as a function of distance Z from the lens.

DISTRIBUTION LIST

DEPARTMENT OF DEFENSE

Assistant Secretary of Defense
Cmd. Cont. Comm. & Intell.
ATTN: M. Epstein

Director
Command Control Technical Center
ATTN: C-312, R. Mason
2 cy ATTN: C-650

Director
Defense Advanced Rsch. Proj. Agency
ATTN: Nuclear Monitoring Research
ATTN: Strategic Tech. Office

Defense Communication Engineer Center
ATTN: Code R410, James W. McLe...

Director
Defense Communications Agency
ATTN: Maurey Raffensperger
ATTN: Code 430
ATTN: Code 810, R. W. Rostron
ATTN: Code 101B

Defense Communications Agency
ATTN: R. L. Crawford

Defense Documentation Center
12 cy ATTN: TC

Director
Defense Intelligence Agency
ATTN: DT-1B
ATTN: DC-7D, W. Wittig

Director
Defense Nuclear Agency
ATTN: TISI Archives
ATTN: STVL
ATTN: DDST
3 cy ATTN: TITL Tech. Lib.
3 cy ATTN: RAHE

Commander, Field Command
Defense Nuclear Agency
ATTN: FCPR

Director
Interservice Nuclear Weapons School
ATTN: Doc. Con.

Director
Joint Strat. Tgt. Planning Staff., JCS
ATTN: JPST, Capt G. D. Goetz
ATTN: JLTH-2

Chief
Livermore Division, Fld. Command, DIA
Lawrence Livermore Laboratory
ATTN: FCPLR

DEPARTMENT OF DEFENSE, (Continued)

Director
National Security Agency
ATTN: W14, Pat Clark
ATTN: Frank Leonard
ATTN: R52, John Skillman

OJCS/J-3
ATTN: WMMCCS, Eval. Ofc., Mr. Toma

Under Sec'y of Def. for Rsch. & Engrg.
ATTN: S&SS (OS)

DEPARTMENT OF THE ARMY

Commander/Director
Atmospheric Sciences Laboratory
U.S. Army Electronics Command
ATTN: DELAS-AE-M, F. E. Niles

Director
BMD Advanced Tech. Ctr.
ATTN: ATC-T, Melvin T. Capps

Chief C-E Services Division
U.S. Army Communications Cmd.
ATTN: CC-OPS-CE

Commander
Harry Diamond Laboratories
ATTN: DRXDO-NP, Cyrus Moazed
ATTN: DRXDO-TI, Mildred H. Weiner
ATTN: DELHD-NP, Francis N. Wimentz
ATTN: DELHD-RB, Robert Williams

Director
TRASANA
ATTN: ATAA-SA
ATTN: TCC, F. Payan, Jr.
ATTN: ATAA-TAC, LTC John Hesse

Director
U.S. Army Ballistic Research Labs.
ATTN: Lawrence J. Puckett

Commander
U.S. Army Comm-Elec. Engrg. Instal. Agcy.
ATTN: EED-PED, George Lane

Commander
U.S. Army Electronics Command
ATTN: DRSEL-MI-RD, H. S. Bennet
ATTN: DRSEL-PL-ENV, Hans A. Bomke

Commander
U.S. Army Foreign Science & Tech. Ctr.
ATTN: R. Jones
ATTN: P. A. Crowley

Commander
U.S. Army Missile Command
ATTN: DRSMI-YTT, W. G. Preussel, Jr.

DEPARTMENT OF THE ARMY (Continued)

Commander
U.S. Army Missile Intelligence Agency
ATTN: Jim Gamble

Commander
U.S. Army Nuclear Agency
ATTN: MOHA-WE, J. Berberet

Commander
U.S. Army Satcom Agency
ATTN: Doc. Con.

DEPARTMENT OF THE NAVY

Chief of Naval Operations
ATTN: OP 943, LCDR Huff
ATTN: Ronald E. Pitkin
ATTN: Alexander Brandt

Chief of Naval Research
ATTN: Code 418
ATTN: Code 461

Commander
Naval Electronic Systems Command
Naval Electronic Systems Cmd. Hqs.
ATTN: PHE 117-T, Satellite Comm. Proj. Off.
ATTN: NAVALEX 034, T. Barry Hughes
ATTN: PHE 117

Commanding Officer
Naval Intelligence Support Ctr.
ATTN: STIC 12, Mr. Dubbin

Commander
Naval Ocean Systems Center
ATTN: Code 0230, C. Baggett
ATTN: Code 532, William F. Moler
3 cy ATN: Code 2200
ATTN: R. Eastman

Director
Naval Research Laboratory
ATTN: Code 7701, Jack D. Brown
ATTN: Code 5400, Hg. Comm. Dir., Bruce Wald
ATTN: Code 7700, Timothy P. Coffey
ATTN: Code 5460, Electromag. Prop. Br.
ATTN: Code 5461, Trans. Inon. Prop.
ATTN: Code 5430, Satellite Comm.
ATTN: Code 5465, Prop. Applications

Commander
Naval Space Surveillance System
ATTN: CAPT J. H. Burton

Officer-in-Charge
Naval Surface Weapons Center
ATTN: Code WA501, Navy Nuc. Orgms. Off.

Commander
Naval Surface Weapons Center
ATTN: R. F. Butler, DF-14

Director
Strategic Systems Project Office
ATTN: NSSP-2722, Fred Wimberly
ATTN: MSP-2141

DEPARTMENT OF THE AIR FORCE

Commander
ADC/DC
ATTN: DC, Mr. Long

Commander
ADCOM/XPD
ATTN: XPQDQ

AF Geophysics Laboratory, AFSC
ATTN: PHD, John P. Mullen
ATTN: OPR, Alva T. Stair
ATTN: OPR, James C. Ulwick
ATTN: LKB, Kenneth S. W. Champion
ATTN: PHD, Jurgen Buchau
ATTN: OPR, Harold Gardner
ATTN: SUOL, Rsch. Lib.
ATTN: PHP, Jules Aarons

AF Weapons Laboratory, AFSC
ATTN: SUL
ATTN: CA, Arthur H. Guenther
ATTN: SAS, John M. Kamm
ATTN: DYC, Capt L. Wittwer

AFTAC
ATTN: TF, Maj Wiley
ATTN: TH

Air Force Avionics Laboratory, AFSC
ATTN: AAD, Allen Johnson

Headquarters
Electronic Systems Division/XR
ATTN: XRC, Lt Col J. Morin
ATTN: XRE, Lt Michaels

Headquarters
Electronic Systems Division/YS
ATTN: YSEV

Headquarters
Electronic Systems Division, AFSC
ATTN: Jim Deas

Commander
Foreign Technology Division, AFSC
ATTN: NICD Library
ATTN: ETD, B. L. Ballard

Hq. USAF/RD
ATTN: RDQ

Commander
Rome Air Development Center, AFSC
ATTN: Y. Coyne Ocse
ATTN: EMTLD, Doc. Lib.

Commander
Rome Air Development Center, AFSC
ATTN: ETEI, A. Lorentzen

SAMSO/MN
ATTN: MNML, Lt Col Kennedy

SAMSO/SK
ATTN: SKA, Lt. Maria A. Clavin

DEPARTMENT OF THE AIR FORCE (Continued)

SANSO/SZ
ATTN: SZJ, Major Lawrence Doan

SANSO/YA
ATTN: YAT, Capt L. Blackwelder

Commander in Chief
Strategic Air Command
ATTN: NRT
ATTN: XPFS, Maj Brian G. Stephan

DEPARTMENT OF ENERGY

EG&G, Inc.
Los Alamos Division
ATTN: James R. Breedlove

University of California
Lawrence Livermore Laboratory
ATTN: Ronald L. Ott, L-531
ATTN: Tech. Info. Dept., L-3
ATTN: Donald R. Dunn, L-156
ATTN: Ralph S. Hager, L-31

Los Alamos Scientific Laboratory
ATTN: Doc. Con. for John Zinn
ATTN: Doc. Con. for R. F. Taschek
ATTN: Doc. Con. for John S. Malik
ATTN: Doc. Con. for Eric Jones

Sandia Laboratories
ATTN: Doc. Con. for D. A. Dahlgren, Org. 1722
ATTN: Doc. Con. for J. P. Martin, Org. 132
ATTN: Doc. Con. for T. Wright
ATTN: Doc. Con. for A. Dean Thornbrough,
Org. 1245
ATTN: Doc. Con. for W. D. Brown, Org 1353

OTHER GOVERNMENT AGENCIES

Department of Commerce
Office of Telecommunications
Institute for Telecom. Science
ATTN: L. A. Berry
ATTN: G. Reed
ATTN: William F. Utlaut

NASA
Goddard Space Flight Center
ATTN: ATS-6, OFC P. Corrigan

National Oceanic & Atmospheric Admin.
Environmental Research Laboratories
Department of Commerce
ATTN: Joseph H. Pope
ATTN: C. L. Rufenach
ATTN: Richard Grubb

DEPARTMENT OF DEFENSE CONTRACTORS

Aerospace Corporation
ATTN: S. P. Bower
ATTN: T. M. Salmi
ATTN: Norman D. Stockwell
ATTN: F. A. Morse, A6, Rm. 2407
ATTN: V. Josephson
ATTN: J. E. Carter, 120, Rm. 2209
ATTN: Irving M. Garfunkel
ATTN: F. E. Bond, A1, Rm. 5003
ATTN: D. P. Olsen, 120, Rm. 2224E

DEPARTMENT OF DEFENSE CONTRACTORS (Continued)

Analytical Systems Engineering Corp.
ATTN: Radio Sciences

The Boeing Company
ATTN: D. Murray
ATTN: Glen Keister

Brown Engineering Company, Inc.
ATTN: Romeo A. Deliberis

University of California at San Diego
Marine Physical Lab. of the Scripps
Institute of Oceanography
ATTN: Henry G. Booker

Charles Stark Draper Laboratory, Inc.
ATTN: J. P. Gilmore, MS 63
ATTN: D. B. Cox

Computer Sciences Corporation
ATTN: Blank

ESL, Inc.
ATTN: J. Roberts
ATTN: C. W. Prettie
ATTN: James Marshall
ATTN: V. L. Mower

Ford Aerospace & Communications Corp.
ATTN: J. T. Mattingley, MS X22

General Electric Company
Space Division
Valley Forge Space Center
ATTN: M. H. Bortner, Space Sci. Lab.

General Electric Company
TEMPO-Center for Advanced Studies
ATTN: Tim Stephens
ATTN: Tom Barrett
ATTN: B. Gambill
ATTN: William McIlamera
ATTN: Warren S. Knapp
ATTN: Mack Stanton
ATTN: Don Chandler
ATTN: DASIAC

General Electric Company
ATTN: F. A. Reibert

General Research Corporation
ATTN: Joel Garbarino
ATTN: John Ise, Jr.

Geophysical Institute
University of Alaska
ATTN: T. H. Davis
ATTN: Neal Brown
ATTN: Tech. Lib.

GTE Sylvania, Inc.
Electronics Systems Grp., Eastern Div.
ATTN: Marshal Cross

HSS, Inc.
ATTN: Donald Hansen

Intl. Tel. & Telegraph Corporation
ATTN: Tech. Lib.

DEPARTMENT OF DEFENSE CONTRACTORS (Continued)

Institute for Defense Analyses

ATTN: Ernest Bauer
ATTN: Joel Bengston
ATTN: Hans Wolfhard
ATTN: J. M. Aein

JAYCOR

ATTN: S. R. Goldman

Johns Hopkins University

Applied Physics Laboratory
ATTN: Document Librarian
ATTN: Thomas Potemra
ATTN: John Dassoulas

Kaman Sciences Corporation

ATTN: B. J. Bittner
ATTN: T. Meagher

Linkabit Corporation

ATTN: Irwin Jacobs

Lockheed Missiles & Space Co., Inc.

ATTN: D. R. Churchill
ATTN: Dept. 60-12

Lockheed Missiles & Space Co., Inc.

ATTN: Richard G. Johnson, Dept. 52-12
ATTN: Martin Walt, Dept. 52-10

M.I.T. Lincoln Laboratory

ATTN: Mr. Walden, X113
ATTN: James H. Pannell, L-246
ATTN: David H. Towle, Lib., A-082
ATTN: D. Clark

McDonnell Douglas Corporation

ATTN: J. Moule
ATTN: George Mroz
ATTN: William Olson
ATTN: H. Harris

Mission Research Corporation

ATTN: Warren A. Schlueter
ATTN: Ralph Kilb
ATTN: R. Hendrick
ATTN: R. Bogusch
ATTN: Dave Sowle
ATTN: F. Fajen
ATTN: W. F. Crevier
ATTN: Steven L. Gutsche
ATTN: D. Sappenfield
ATTN: D. L. Knepp

5 cy ATTN: Tech. Lib.

The Mitre Corporation

ATTN: C. E. Callahan
ATTN: Chief Scientist, W. Sen
ATTN: G. Harding

DEPARTMENT OF DEFENSE CONTRACTORS (Continued)

Pacific-Sierra Research Corp.

ATTN: E. C. Field, Jr.

Photometrics, Inc.

ATTN: Irving L. Kofsky

Physical Dynamics, Inc.

ATTN: Joseph B. Workman
ATTN: A. Thompson

R & D Associates

ATTN: William J. Karzas
ATTN: William B. Wright, Jr.
ATTN: Forrest Gilmore
ATTN: Robert E. Lelevier
ATTN: Bryan Gabbard

The Rand Corporation

ATTN: Ed Bedrozian
ATTN: Cullen Crain

Raytheon Company

ATTN: Barbara Adams

Science Applications, Inc.

ATTN: E. A. Straker
ATTN: Daniel A. Hamlin
ATTN: Curtis A. Smith
ATTN: D. Sachs
ATTN: Lewis M. Linson
ATTN: Jack McDougall

Science Applications, Inc.

Huntsville Division
ATTN: Dale H. Davis

SRI International

ATTN: Alan Burns
ATTN: Walter G. Chesnut
ATTN: Charles L. Rino
ATTN: Ray L. Leadabrand
ATTN: Walter Jaye
ATTN: M. Baron
ATTN: L. L. Cobb
ATTN: Donald Neilson

Technology International Corporation

ATTN: W. P. Boquist

TRW Defense & Space Sys. Group

ATTN: R. K. Plebuch, R1-2078

Visidyne, Inc.

ATTN: Charles Humphrey
ATTN: J. W. Carpenter